



Calculation of predictions for non-identical particle correlations in heavy ions collisions at LHC energies from hydrodynamics-inspired models

MASTER OF SCIENCE THESIS

Author:
Mateusz Wojciech Gałażyn

Supervisor:
Prof. Adam Kisiel

Warsaw, 17th November 2014



Wyznaczenie przewidywań teoretycznych dla korelacji cząstek nieidentycznych w zderzeniach ciężkich jonów przy energiach LHC w modelach opartych na hydrodynamice

PRACA MAGISTERSKA

Autor:
Mateusz Wojciech Gałażyn

Promotor:
dr hab. inż. Adam Kisiel, prof. PW

Warszawa, 17 listopada 2014

1 Abstract

2 This thesis presents results of two-particle momentum correlations analysis
3 for different kinds of particles produced in heavy ion collisions. The studies
4 were carried for the data from lead-lead collisions at the centre of mass
5 energy $\sqrt{s_{NN}} = 2.76$ TeV simulated in the THERMINATOR model using the
6 (3+1)-dimensional hydrodynamic model with viscosity. Analysis was performed
7 for the three particle kinds: pions, kaons and protons for the collisions in eight
8 different centrality ranges.

9 The THERMINATOR model allows to perform statistical hadronization of
10 stable particles and unstable resonances from a given hypersurface which is
11 followed by the resonance propagation and decay phase. The four-dimensional
12 hypersurface is coming from the calculations performed on a basis of relativistic
13 hydrodynamic framework with the viscosity corrections.

14 One can investigate space-time characteristics of the particle-emitting source
15 through two-particle interferometry using experimental observables. The
16 experimental-like analysis of the data coming from a model calculations yields
17 a possibility to test the hydrodynamic description of a quark-gluon plasma.
18 This thesis concentrates on the verification of the prediction of appearance of
19 femtoscopic radii scaling with the transverse mass.

20 The three dimensional correlation functions were calculated using spherical
21 harmonics decomposition. One can use this approach to perform calculations
22 with the less statistics and the visualization of results is much easier. The calcu-
23 lated correlation functions show expected increase of a correlation for pions and
24 kaons at the low relative momenta of a pair. For the protons at the same mo-
25 mentum region, the decrease occurs. The transverse pair momentum and cen-
26 tralitity dependence on a correlation function is observed. In order to perform the
27 quantitative analysis of this influence, the fitting of theoretical formula for cor-
28 relation function was performed. The femtoscopic radii calculated in the LCMS
29 and PRF are falling with the transverse mass m_T . To test the scaling predicted
30 from the hydrodynamics, the power law was fitted $\alpha m_T^{-\beta}$. The radii calculated
31 for pions, kaons and protons in the LCMS are following the common scaling. In
32 case of the PRF no such scaling is observed. To recover the scaling in the PRF, the
33 approximate factor to recover scaling is proposed: $\sqrt{(\sqrt{\gamma_T} + 2)/3}$. The radii in
34 the PRF divided by the proposed scaling factor are falling on the common curve,
35 therefore the scaling can be recovered using the proposed scaling factor. The
36 experimental analysis is usually performed in the PRF (requires less statistics),
37 hence the method of scaling recovery enables easier testing of the hydrodynamic
38 predictions, which are not visible in the PRF.

Streszczenie

40 W tej pracy zaprezentowane są wyniki analizy dwucząstkowych korelacji pę-
41 dowych dla trzech różnych typów cząstek produkowanych w zderzeniach cięż-
42 kich jonów. Obliczenia zostały wykonane dla danych ze zderzeń ołów-ołów przy
43 energii w centrum masy $\sqrt{s_{NN}} = 2.76$ TeV wygenerowanych za pomocą mo-
44 delu THERMINATOR przy użyciu (3+1)-wymiarowego modelu hydrodynamicz-
45 nego uwzględniającego lepkość ośrodka. Analiza została wykonana dla trzech
46 rodzajów cząstek: pionów, kaonów i protonów dla dziewięciu różnych przedzia-
47 łów centralności.

48 Model THERMINATOR pozwala na wykonanie statystycznej hadronizacji
49 stabilnych cząstek jak i również niestabilnych rezonansów z danej
50 hiperpowierzchni wymrażania oraz uwzględnienie propagacji i rozpadów
51 tych rezonansów. Czterowymiarowa hiperpowierzchnia pochodzi z
52 obliczeń przeprowadzonych na podstawie hydrodynamiki relatywistycznej z
53 uwzględnieniem poprawek pochodzących od lepkości.

54 Interferometria dwucząstkowa pozwala na zbadanie charakterystyk
55 czasowo-przestrzennych źródła cząstek. Poprzez analizę danych pochodzących
56 z obliczeń modelowych można dokonać sprawdzenia zakresu stosownalności
57 hydrodynamiki do opisu właściwości plazmy kwarkowo-gluonowej. Ta praca
58 koncentruje się na weryfikacji skalowania promieni femtoskopowych z masą
59 poprzeczną przewidywanego przez hydrodynamikę.

60 Trójwymiarowe funkcje korelacyjne zostały obliczone za pomocą rozkładu w
61 szeregu harmonik sferycznych. To podejście wymaga mniejszej statystyki i po-
62 zwala na łatwiejszą wizualizację wyników. Obliczone funkcje korelacyjne wy-
63 kazują oczekiwany wzrost korelacji dla niskich różnic pędów dla par pionów i
64 kaonów. Dla par protonów w tym samym zakresie pędów widoczny jest spa-
65 dek korelacji. Widoczny jest wpływ pędu poprzecznego pary oraz centralności
66 na funkcję korelacyjną. W celu wykonania analizy ilościowej tego wpływu, zo-
67 stało wykonane dopasowanie teoretycznych funkcji korelacyjnych do tych obli-
68 czonych na podstawie danych eksperimentalnych. Promienie femtoskopowe w
69 LCMS i PRF wykazują spadek wraz z wzrostem masy poprzecznej m_T . W celu
70 sprawdzenie skalowania przewidywanego przez hydrodynamikę została dopa-
71 sowana zależność potęgowa: $\alpha m_T^{-\beta}$. Promienie obliczone dla pionów, kaonów i
72 protonów zachowują wzajemne skalowanie w LCMS. W przypadku PRFu7wzd
73 skalowanie nie jest widoczne. Aby odzyskać skalowanie w PRF, został zapro-
74 ponowany przybliżony współczynnik: $\sqrt{(\sqrt{\gamma_T} + 2)/3}$. Promienie w PRF po
75 podzieleniu przez współczynnik skalowania, są opisywalne przez podaną za-
76 leżność potęgową, zatem umożliwia on odzyskanie skalowania. Analiza ekspe-
77 rymentalna jest zazwyczaj wykonywana w PRF (wymaga mniejszej statystyki),

⁷⁸ zatem ta metoda pozwala na łatwiejszą weryfikację przewidywań hydrodyna-
⁷⁹ miki które nie są widoczne w PRF.

⁸⁰ Contents

⁸¹	Introduction	1
⁸²	1 Theory of heavy ion collisions	3
⁸³	1.1 The Standard Model	3
⁸⁴	1.2 Quantum Chromodynamics	4
⁸⁵	1.2.1 Quarks and gluons	4
⁸⁶	1.2.2 Quantum Chromodynamics potential	5
⁸⁷	1.2.3 The quark-gluon plasma	7
⁸⁸	1.3 Relativistic heavy ion collisions	8
⁸⁹	1.3.1 Stages of heavy ion collision	8
⁹⁰	1.3.2 QGP signatures	10
⁹¹	2 Therminator model	18
⁹²	2.1 (3+1)-dimensional viscous hydrodynamics	18
⁹³	2.2 Statistical hadronization	19
⁹⁴	2.2.1 Cooper-Frye formalism	20
⁹⁵	3 Particle interferometry	22
⁹⁶	3.1 HBT interferometry	22
⁹⁷	3.2 Theoretical approach	23
⁹⁸	3.2.1 Conventions used	23
⁹⁹	3.2.2 Two particle wave function	24
¹⁰⁰	3.2.3 Source emission function	25
¹⁰¹	3.2.4 Theoretical correlation function	27
¹⁰²	3.2.5 Spherical harmonics decomposition of a correlation function	28
¹⁰³	3.3 Experimental approach	29
¹⁰⁴	3.4 Scaling of femtoscopic radii	30
¹⁰⁵	3.4.1 Scaling in LCMS	31
¹⁰⁶	3.4.2 Scaling in PRF	31
¹⁰⁷	4 Results	33
¹⁰⁸	4.1 Identical particles correlations	33
¹⁰⁹	4.1.1 Spherical harmonics components	33
¹¹⁰	4.1.2 Centrality dependence of a correlation function	37

111	4.1.3	k_T dependence of a correlation function	38
112	4.2	Results of the fitting procedure	39
113	4.2.1	The three-dimensional femtoscopic radii scaling	39
114	4.2.2	Scaling of one-dimensional radii	43
115	4.3	Discussion of the results	44
116	Conclusions		45

¹¹⁷ Introduction

¹¹⁸ Many people were trying to discover what was before the universe which we
¹¹⁹ observe today. Through the years there were appearing more or less successful
¹²⁰ theories which were trying to describe its origin and behaviour. Among them
¹²¹ is one model, which provides a comprehensive explanation for a broad range
¹²² of phenomena, including the cosmic microwave background, abundance of the
¹²³ light elements and Hubble's law. This model is called The Big Bang theory and
¹²⁴ has born in the 1927 on the basis of principles proposed by the Belgian priest and
¹²⁵ scientist Georges Lemaître. Using this model and known laws of physics one can
¹²⁶ calculate the characteristics of the universe in detail back in time to the extreme
¹²⁷ densities and temperatures. However, at some point these calculations fail. The
¹²⁸ extrapolation of the expansion of universe backwards in time using general re-
¹²⁹ lativity yields an infinite density and temperature at a finite time in the past. This
¹³⁰ appearance of singularity is a signal of the breakdown of general relativity. The
¹³¹ range of this extrapolation towards singularity is debated - certainly we can go
¹³² no closer than the end of *Planck epoch* i.e. 10^{-43} s. At this very first era the tem-
¹³³ perature of the universe was so high, that the four fundamental forces - electro-
¹³⁴ magnetism, gravitation, weak nuclear interaction and strong nuclear interaction
¹³⁵ - were one fundamental force. Between 10^{-43} s and 10^{-36} s of a lifetime of the
¹³⁶ universe, there is a *grand unification epoch*, at which forces are starting to separate
¹³⁷ from each other. From 10^{-36} s to 10^{-12} s lasted *electroweak epoch*, when the strong
¹³⁸ force separated from the electroweak force. After the electroweak epoch, there
¹³⁹ was the *quark epoch* in which the universe was a dense "soup" of quarks. During
¹⁴⁰ this stage the fundamental forces of gravitation, electromagnetism, strong and
¹⁴¹ weak interactions had taken their present forms. The temperature at this mo-
¹⁴² ment was still too high to allow quarks to bind together and form hadrons. At
¹⁴³ the end of quark era, there was a big freeze-out - when the average energy of
¹⁴⁴ particle interactions had fallen below the binding energy of hadrons. This era in
¹⁴⁵ which quarks became confined into hadrons is known as the hadron epoch. At
¹⁴⁶ this moment the matter had started forming nuclei and atoms, which we observe
¹⁴⁷ today.

¹⁴⁸ Here arises the question: how we can study the very beginning of the
¹⁴⁹ universe? To do this, one should create in a laboratory a system with a such
¹⁵⁰ large density and high temperature to recreate those conditions. Today, this is
¹⁵¹ achievable through sophisticated machines, which are particle accelerators. In

152 the particle accelerators, like the Large Hadron Collider at CERN, Geneva or
153 Relativistic Heavy Ion Collider at Brookhaven National Laboratory in Upton,
154 New York, the heavy ions after being accelerated to the near speed of light are
155 collided in order to generate extremely dense and hot phase of matter and
156 recreate the quark-gluon plasma. The plasma is believed to behave like an
157 almost ideal fluid and to become a medium, that can be described by the laws of
158 relativistic hydrodynamics.

159 This thesis is a verification of predictions for collective behaviour of the
160 quark-gluon plasma coming from the hydrodynamic equations using the
161 experimental-like analysis for the high energy Pb-Pb collisions generated using
162 the THERMINATOR model.

163 The 1st chapter is an introduction to the theory of heavy ion collisions. It
164 contains the brief description of the Standard Model and Quantum Chromody-
165 namics. The quark-gluon plasma and its signatures are also characterized.

166 In the 2nd chapter there is a description of the relativistic hydrodynamic
167 framework and the THERMINATOR model used to perform the simulations of col-
168 lisions.

169 The 3rd chapter covers the particle interferometry method used in this work.
170 The algorithm of building experimental correlation functions and effects coming
171 from the hydrodynamics in the experimental results for particle interferometry
172 are also presented.

173 In the 4th chapter there is a detailed analysis of the results for two-particle
174 femtoscopy for different pairs of particles. The quantitative analysis of calcu-
175 lated femtoscopic radii as well as the appearance of transverse mass scaling is
176 discussed.

¹⁷⁷ **Chapter 1**

¹⁷⁸ **Theory of heavy ion collisions**

¹⁷⁹ **1.1 The Standard Model**

¹⁸⁰ In the 1970s, a new theory of fundamental particles and their interaction
¹⁸¹ emerged. A new concept, which concerns the electromagnetic, weak and strong
¹⁸² nuclear interactions between known particles. This theory is called *The Standard*
¹⁸³ *Model*. There are seventeen named particles in the standard model, organized
¹⁸⁴ into the chart shown below (Fig. 1.1). Fundamental particles are divided into
two families: *fermions* and *bosons*.

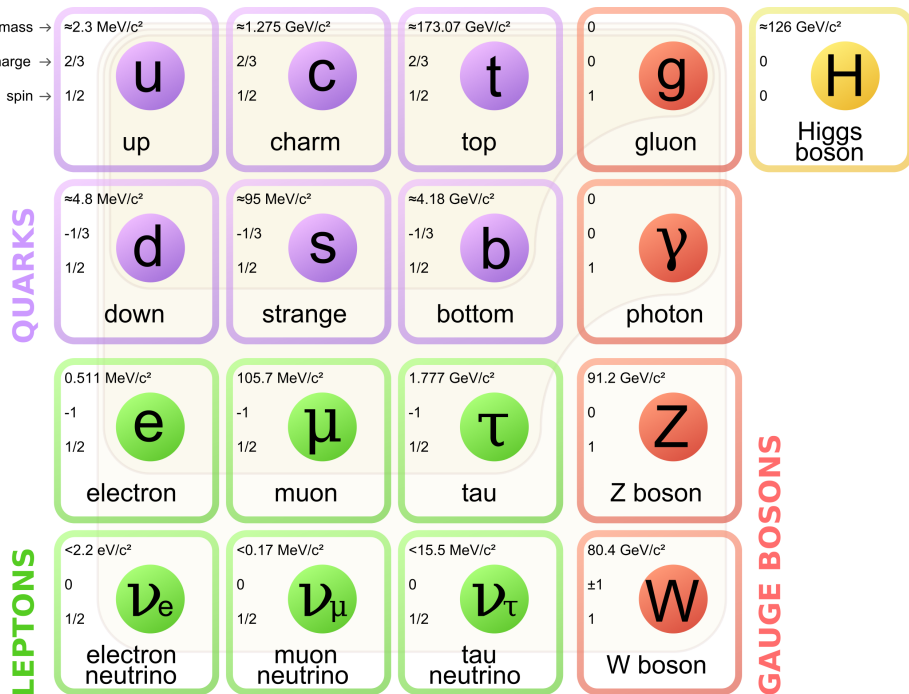


Figure 1.1: The Standard Model of elementary particles [1].

185 Fermions are the building blocks of matter. They are divided into two groups.
 186 Six of them, which must bind together are called *quarks*. Quarks are known to
 187 bind into doublets (*mesons*), triplets (*baryons*) and recently confirmed four-quark
 188 states.¹ Two of baryons, with the longest lifetimes, are forming a nucleus: a pro-
 189 ton and a neutron. A proton is build from two up quarks and one down, and
 190 neutron consists of two down quarks and one up. A proton is found to be a stable
 191 particle (at least it has a lifetime larger than 10^{35} years) and a free neutron has a
 192 mean lifetime about 8.8×10^2 s. Fermions, that can exist independently are called
 193 *leptons*. Neutrinos are a subgroup of leptons, which are only influenced by weak
 194 interaction. Fermions can be divided into three generations (three columns in
 195 the Figure 1.1). Generation I particles can combine into hadrons with the longest
 196 life spans. Generation II and III consists of unstable particles which form also
 197 unstable hadrons.

198 Bosons are force carriers. There are four fundamental forces: weak - respons-
 199 ible for radioactive decay, strong - coupling quarks into hadrons, electromagnetic
 200 - between charged particles and gravity - the weakest, which causes the attraction
 201 between particles with a mass. The Standard Model describes the first three. The
 202 weak force is mediated by W^\pm and Z^0 bosons, electromagnetic force is carried by
 203 photons γ and the carriers of a strong interaction are gluons g . The fifth boson is
 204 a Higgs boson which is responsible for giving other particles mass.

205 1.2 Quantum Chromodynamics

206 1.2.1 Quarks and gluons

207 Quarks interact with each other through the strong interaction. The mediator
 208 of this force is a *gluon* - a massless and chargeless particle. In the quantum chro-
 209 modynamics (QCD) - theory describing strong interaction - there are six types of
 210 "charges" (like electrical charges in the electrodynamics) called *colours*. The col-
 211 ours were introduced because some of the observed particles, like Δ^- , Δ^{++} and
 212 Ω^- appeared to consist of three quarks with the same flavour (ddd , uuu and sss
 213 respectively), which was in conflict with the Pauli principle. One quark can carry
 214 one of the three colours (usually called *red*, *green* and *blue*) and antiquark one of
 215 the three anti-colours respectively. Only colour-neutral (or white) particles could
 216 exist. Mesons are assumed to be a colour-anticolour pair, while baryons are *red-*
 217 *green-blue* triplets. Gluons also are colour-charged and there are 8 types of gluons.
 218 Therefore they can interact with themselves [3].

¹The LHCb experiment at CERN in Geneva confirmed recently existence of $Z(4430)$ - a particle consisting of four quarks [2].

219 **1.2.2 Quantum Chromodynamics potential**

220 As a result of that gluons are massless, one can expect, that the static potential
 221 in the QCD will have the similar form like one in the electrodynamics e.g. $\sim 1/r$
 222 (through an analogy to photons). In reality the QCD potential is assumed to have
 223 the form of [3]

$$V_s = -\frac{4}{3} \frac{\alpha_s}{r} + kr, \quad (1.1)$$

224 where the α_s is a coupling constant of the strong force and the kr part is related
 225 with the *confinement*. In comparison to the electromagnetic force, a value of the
 226 strong coupling constant is $\alpha_s \approx 1$ and the electromagnetic one is $\alpha = 1/137$.

227 The fact that quarks does not exist separately, but they are always bound,
 228 is called a confinement. As two quarks are pulled apart, the linear part kr in
 229 the Eq. 1.1 becomes dominant and the potential becomes proportional to the dis-
 230 tance. This situation resembles stretching of a string. At some point, when the
 231 string is so large it is energetically favourable to create a quark-antiquark pair. At
 232 this moment such pair (or pairs) is formed, the string breaks and the confinement
 233 is preserved (Fig. 1.2).

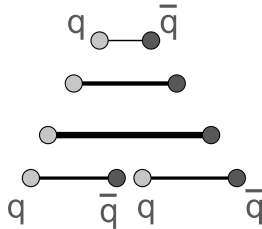


Figure 1.2: A string break and a creation of a pair quark-anti-quark [4].

233 On the other hand, for the small r , an interaction between the quarks and
 234 gluons is dominated by the Coulomb-like term $-\frac{4}{3} \frac{\alpha_s}{r}$. The coupling constant α_s
 235 depends on the four-momentum Q^2 transferred in the interaction. This depend-
 236 ence is presented in Fig. 1.3. The value α_s decreases with increasing momentum
 237 transfer and the interaction becomes weak for large Q^2 , i.e. $\alpha_s(Q) \rightarrow 0$. Be-
 238 cause of weakening of coupling constant, quarks at large energies (or small dis-
 239 tances) are starting to behave like free particles. This phenomenon is known as
 240 an *asymptotic freedom*. The QCD potential has also temperature dependence - the
 241 force strength “melts” with the temperature increase. Therefore the asymptotic
 242 freedom is expected to appear in either the case of high baryon densities (small
 243 distances between quarks) or very high temperatures. This temperature depend-
 244 ence is illustrated in the Fig. 1.4.

245 If the coupling constant α_s is small, one can use perturbative methods to cal-
 246 culate physical observables. Perturbative QCD (pQCD) successfully describes
 247 hard processes (with large Q^2), such as jet production in high energy proton-
 248 antiproton collisions. The applicability of pQCD is defined by the *scale parameter*

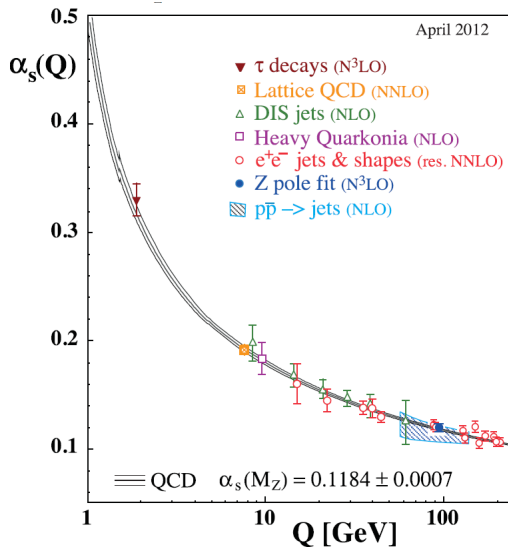


Figure 1.3: The coupling parameter α_s dependence on four-momentum transfer Q^2 [5].

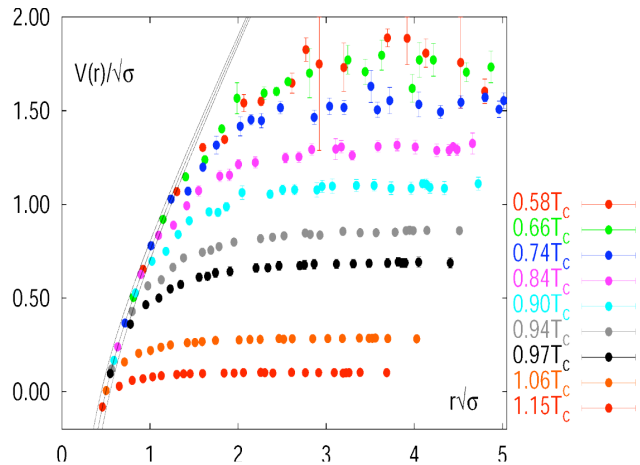


Figure 1.4: The QCD potential for a pair quark-antiquark as a function of distance for different temperatures. A value of a potential decreases with the temperature [4].

250 $\Lambda_{QCD} \approx 200$ MeV. If $Q \gg \Lambda_{QCD}$ then the process is in the perturbative domain
 251 and can be described by pQCD. A description of soft processes (when $Q < 1$ GeV)
 252 is a problem in QCD - perturbative theory breaks down at this scale. Therefore,
 253 to describe processes with low Q^2 , one has to use alternative methods like Lattice
 254 QCD. Lattice QCD (LQCD) is non-perturbative implementation of a field theory
 255 in which QCD quantities are calculated on a discrete space-time grid. LQCD al-

lows to obtain properties of matter in equilibrium, but there are some limitations. Lattice QCD requires fine lattice spacing to obtain precise results - therefore large computational resources are necessary. With the constant growth of computing power this problem will become less important. The second problem is that lattice simulations are possible only for baryon density $\mu_B = 0$. At $\mu_B \neq 0$, Lattice QCD breaks down because of the sign problem [6].

1.2.3 The quark-gluon plasma

The new state of matter in which quarks are no longer confined is known as a *quark-gluon plasma* (QGP). The predictions coming from the discrete space-time Lattice QCD calculations reveal a phase transition from the hadronic matter to the quark-gluon plasma at the high temperatures and baryon densities. The res-

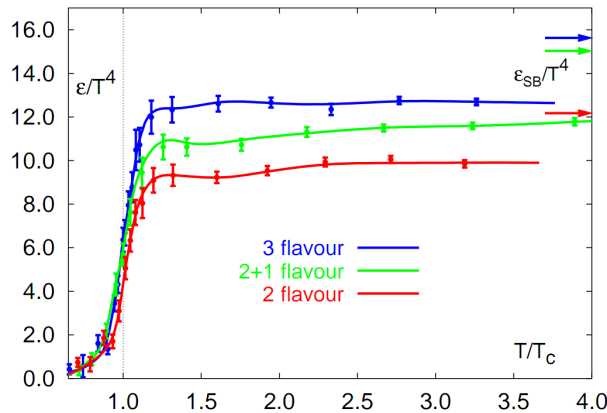


Figure 1.5: A number of degrees of freedom as a function of a temperature [7].

ults obtained from such calculations are shown on Fig. 1.5. The energy density ϵ which is divided by T^4 is a measure of number of degrees of freedom in the system. One can observe significant rise of this value, when the temperature increases past the critical value T_C . Such increase is signaling a phase transition - the formation of QGP [8]. The values of the energy densities plotted in Fig. 1.5 do not reach the Stefan-Boltzmann limit ϵ_{SB} (marked with arrows), which corresponds to an ideal gas. This can indicate some residual interactions in the system. According to the results from the RHIC², the new phase of matter behaves more like an ideal fluid, than like a gas [9].

One of the key questions, to which current heavy ion physics tries to find an answer is the value of a critical temperature T_C as a function of a baryon chemical potential μ_B (baryon density), where the phase transition occur. The results coming from the Lattice QCD are presented in the Fig. 1.6. The phase of matter in which quarks and gluons are deconfined is expected to exist at large

²Relativistic Heavy Ion Collider at Brookhaven National Laboratory in Upton, New York

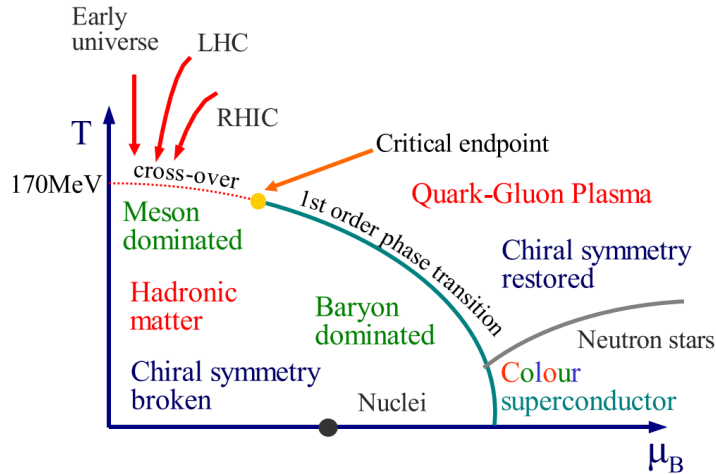


Figure 1.6: Phase diagram coming from the Lattice QCD calculations [8].

temperatures. In the region of small temperatures and high baryon densities, a different state is supposed to appear - a *colour superconductor*. The phase transition between hadronic matter and QGP is thought to be of 1st order at $\mu_B \gg 0$. However as $\mu_B \rightarrow 0$ quarks' masses become significant and a sharp transition transforms into a rapid but smooth cross-over. It is believed that in Pb-Pb collisions observed at the LHC³, the created matter has high enough temperature to be in the quark-gluon plasma phase, then cools down and converts into hadrons, undergoing a smooth transition [8].

1.3 Relativistic heavy ion collisions

1.3.1 Stages of heavy ion collision

To create the quark-gluon plasma one has to achieve high enough temperatures and baryon densities. Such conditions can be recreated in the heavy ion collisions at the high energies. The left side of the Figure 1.7 shows simplified picture of a central collision of two highly relativistic nuclei in the centre-of-mass reference frame. The colliding nuclei are presented as thin disks because of the Lorentz contraction. In the central region, where the energy density is the highest, a new state of matter - the quark-gluon plasma - is supposedly created. Afterwards, the plasma expands ad cools down, quarks combine into hadrons and their mutual interactions cease when the system reaches the *freeze-out* temperature. Subsequently, produced free hadrons move towards the detectors.

On the right side of the Figure 1.7 there is presented a space-time evolution of a collision process, plotted in the light-cone variables (z, t). The two highly

³Large Hadron Collider at CERN, Geneva

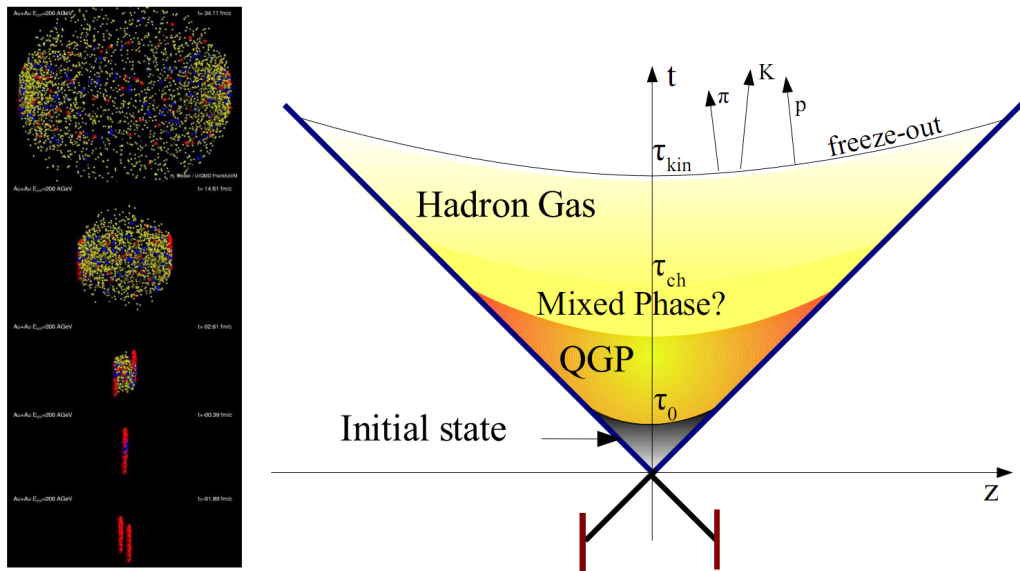


Figure 1.7: Left: stages of a heavy ion collision simulated in the UrQMD model. Right: schematic view of a heavy ion collision evolution [8].

303 relativistic nuclei are traveling basically along the light cone until they collide
 304 at the centre of diagram. Nuclear fragments emerge from the collision again
 305 along the (forward) light cone, while the matter between fragmentation zones
 306 populates the central region. This hot and dense matter is believed to be in the
 307 state of the quark-gluon plasma. There exist several frameworks to describe this
 308 transition to the QGP phase, for example: QCD string breaking, QCD parton cas-
 309 cades or colour glass condensate evolving into glasma and later into quark-gluon
 310 plasma [10].

311 **String breaking** – In the string picture, the nuclei pass through each other forming
 312 colour strings. This is analogous to the situation depicted in the Fig 1.2 - the
 313 colour string is created between quarks inside particular nucleons in nuclei. In
 314 the next step strings decay / fragment forming quarks and gluons or directly
 315 hadrons. This approach becomes invalid at very high energies, when the strings
 316 overlap and cannot be treated as independent objects.

317 **Parton cascade** – The parton⁴ cascade model is based on the pQCD. The col-
 318 liding nuclei are treated as clouds of quarks and which penetrate through each
 319 other. The key element of this method is the time evolution of the parton phase-
 320 space distributions, which is governed by a relativistic Boltzmann equation with
 321 a collision term that contains dominant perturbative QCD interations. The bot-
 322 tleneck of the parton cascade model is the low energies regime, where the Q^2 is
 323 too small to be described by the perturbative theory.

⁴A parton is a common name for a quark and a gluon.

324 **Colour glass condensate** – The colour glass condensate assumes, that the had-
 325 ion can be viewed as a tightly packed system of interacting gluons. The sat-
 326 uration of gluons increases with energy, hence the total number of gluons may
 327 increase without the bound. Such a saturated and weakly coupled gluon system
 328 is called a colour glass condensate. The fast gluons in the condensate are Lorentz
 329 contracted and redistributed on the two very thin sheets representing two col-
 330 liding nuclei. The sheets are perpendicular to the beam axis. The fast gluons
 331 produce mutually orthogonal colour magnetic and electric fields, that only ex-
 332 ist on the sheets. Immediately after the collision, i.e. just after the passage of
 333 the two gluonic sheets after each other, the longitudinal electric and magnetic
 334 fields are produced forming the *glasma*. The glasma fields decay through the
 335 classical rearrangement of the fields into radiation of gluons. Also decays due to
 336 the quantum pair creations are possible. In this way, the quark-gluon plasma is
 337 produced.

338 Interactions within the created quark-gluon plasma bring the system into the
 339 local statistical equilibrium, hence its further evolution can be described by the
 340 relativistic hydrodynamics. The hydrodynamic expansion causes that the sys-
 341 tem becomes more and more dilute. The phase transition from the quark-gluon
 342 plasma to the hadronic gas occurs. Further expansion causes a transition from the
 343 strongly interaction hadronic gas to weakly interacting system of hadrons which
 344 move freely to the detectors. Such decoupling of hadrons is called the *freeze-out*.
 345 The freeze-out can be divided into two phases: the chemical freeze-out and the
 346 thermal one. The *chemical freeze-out* occurs when the inelastic collisions between
 347 constituents of the hadron gas stop. As the system evolves from the chemical
 348 freeze-out to the thermal freeze-out the dominant processes are elastic collisions
 349 (such as, for example $\pi + \pi \rightarrow \rho \rightarrow \pi + \pi$) and strong decays of heavier reso-
 350 nances which populate the yield of stable hadrons. The *thermal freeze-out* is the
 351 stage of the evolution of matter, when the strongly coupled system transforms
 352 to a weakly coupled one (consisting of essentially free particles). In other words
 353 this is the moment, where the hadrons practically stop to interact. Obviously, the
 354 temperatures corresponding to the two freeze-outs satisfy the condition

$$T_{chem} > T_{therm}, \quad (1.2)$$

355 where T_{chem} (inferred from the ratios of hadron multiplicities) is the temperature
 356 of the chemical freeze-out, and T_{therm} (obtained from the investigation of the
 357 transverse-momentum spectra) is the temperature of the thermal freeze-out [10].

358 1.3.2 QGP signatures

359 The quark-gluon plasma is a very short living and unstable state of matter.
 360 One cannot investigate the properties of a plasma and confirm its existence dir-
 361 ectly. Hence, the several experimental effects were proposed as QGP signatures,
 362 some of them have been already observed in heavy ion experiments [8]. As mat-
 363 ter created in the heavy ions collisions is supposed to behave like a fluid, one

should expect appearance of collective behaviour at small transverse momenta - so called *elliptic flow* and *radial flow*. The next signal is the temperature range obtained from the measurements of *direct photons*, which gives us information, that the system created in heavy ion collisions is far above the critical temperature obtained from the LQCD calculations. The *puzzle in the di-lepton spectrum* can be explained by the modification of spectral shape of vector mesons (mostly ρ meson) in the presence of a dense medium. This presence of a medium can also shed light on the *jet quenching* phenomenon - the suppression occurrence in the high p_T domain.

Elliptic flow

In a non-central heavy ion collisions, created region of matter has an almond shape with its shorter axis in the *reaction plane* (Fig. 1.8). The pressure gradient is much larger in-plane rather than out-of-plane. This causes larger acceleration and transverse velocities in-plane rather than out-of-plane. Such differences can

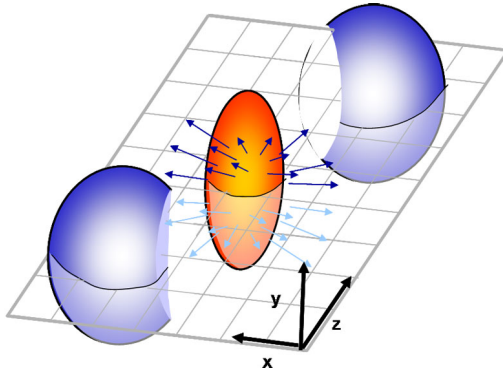


Figure 1.8: Overlapping region which is created in heavy ion collisions has an almond shape. Visible x-z plane is a *reaction plane*. The x-y plane is a *transverse plane*. The z is a direction of the beam [11].

be investigated by studying the distribution of particles with respect to the reaction plane orientation [12]:

$$E \frac{d^3 N}{dp^3} = \frac{1}{2\pi} \frac{d^2 N}{p_T dp_T dy} (1 + 2v_1 \cos(\phi) + 2v_2 \cos(2\phi) + \dots), \quad (1.3)$$

where ϕ is the angle between particle transverse momentum p_T (a momentum projection on a transverse plane) and the reaction plane, N is a number of particles and E is an energy of a particle. The y variable is a *rapidity* defined as:

$$y = \frac{1}{2} \ln \left(\frac{E + p_L}{E - p_L} \right), \quad (1.4)$$

383 where p_L is a longitudinal component of a momentum (parallel to the beam direction).
 384 The v_n coefficients indicate the shape of a system. For the most central collisions
 385 ($b = 0$ - see Fig. 1.9) all coefficients vanish $\bigwedge_{n \in N_+} v_n = 0$ (the overlapping region has the spherical shape). The Fourier series elements in the parentheses

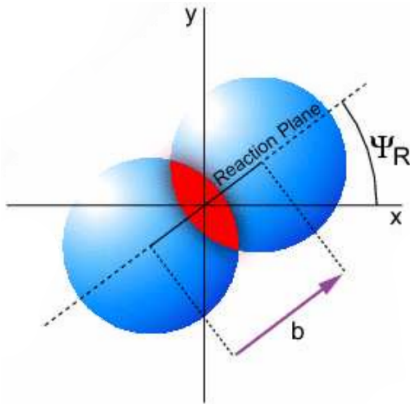


Figure 1.9: Cross-section of a heavy ion collision in a transverse plane. Ψ_R is an angle between transverse plane and the reaction plane. The b parameter is an *impact parameter* - a distance between centers of nuclei during a collision. An impact parameter is related with the centrality of a collision and a volume of the quark-gluon plasma [12].

386 in Eq. 1.3 represent different kinds of a flow. The first value: "1" represents the
 387 *radial flow* - an isotropic flow in every direction. Next coefficient v_1 is responsible
 388 for *direct flow*. The v_2 coefficient is a measure of elliptic anisotropy (*elliptic flow*).
 389 The v_2 has to build up in the early stage of a collision - later the system becomes
 390 too dilute: space asymmetry and the pressure gradient vanish. Therefore the
 391 observation of elliptic flow means that the created matter was in fact a strongly
 392 interacting matter.

393 The v_2 coefficient was measured already at CERN SPS, LHC and RHIC. For
 394 the first time hydrodynamics successfully described the collision dynamics as the
 395 measured v_2 reached hydrodynamic limit (Fig. 1.10). As expected, there is a mass
 396 ordering of v_2 as a function of p_T (lower plot in the Fig. 1.10) with pions having
 397 the largest and protons the smallest anisotropy. In the upper plots in the Fig. 1.10
 398 there is a v_2 as a function of transverse kinetic energy. The left plot shows the
 399 two universal trend lines for baryons and mesons. After the scaling of v_2 and the
 400 kinetic energy by the number of valence quarks, all of the hadrons follow the
 401 same universal curve. Those plots show that strong collectivity is observed in
 402 heavy ion collisions.

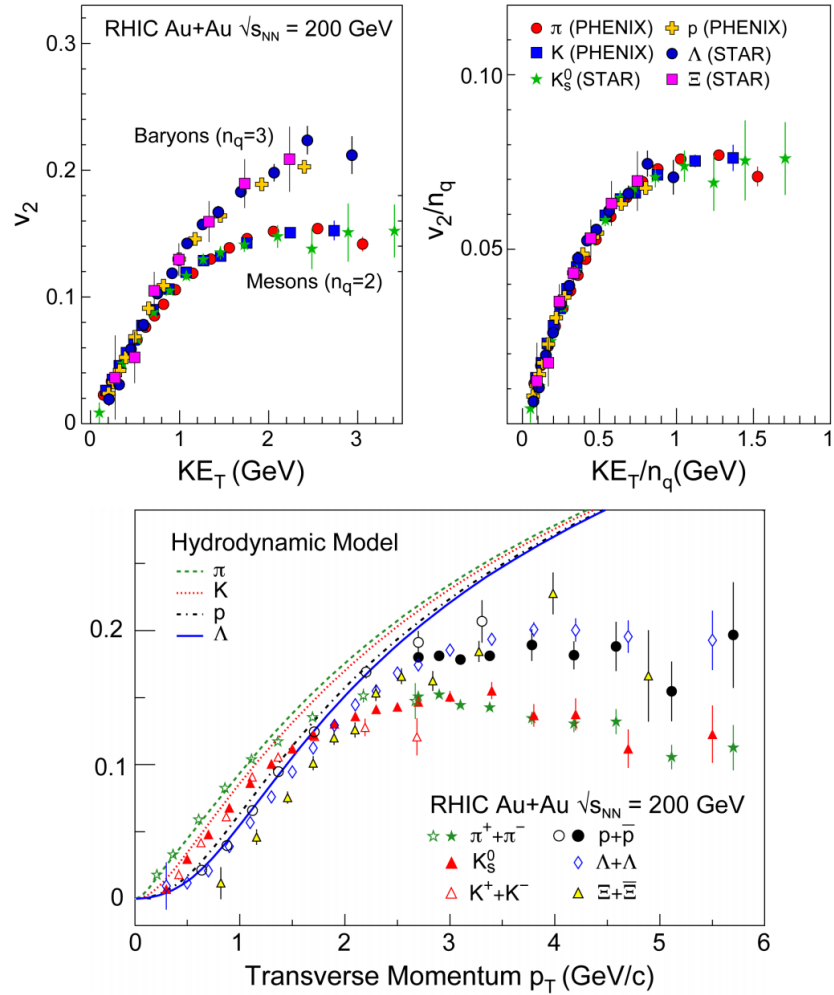


Figure 1.10: *Lower:* The elliptic flow v_2 follows the hydrodynamical predictions for an ideal fluid perfectly. Note that > 99% of all final hadrons have $p_T < 1.5$ GeV/c. *Upper left:* The v_2 plotted versus transverse kinetic energy $KE_T = m_T - m_0 = \sqrt{p_T^2 + m_0^2} - m_0$. The v_2 follows different universal curves for mesons and baryons. *Upper right:* When scaled by the number of valence quarks, the v_2 follows the same universal curve for all hadrons and for all values of scaled transverse kinetic energy [13].

404 Transverse radial flow

405 Elliptic flow described previously is caused by the pressure gradients which
 406 must also produce a more simple collective behaviour of matter - a movement
 407 inside-out, called radial flow. Particles are pushed to higher momenta and they
 408 move away from the center of the collision. A source not showing collective

409 behaviour, like pp collisions, produces particle spectra that can be fitted by a
 410 power-law [8]:

$$\frac{1}{2\pi p_T} \frac{d^2N}{dp_T d\eta} = C \left(1 + \frac{p_T}{p_0} \right)^{-\gamma}. \quad (1.5)$$

411 The η variable is a *pseudorapidity* defined as follows:

$$\eta = \frac{1}{2} \ln \left(\frac{p + p_L}{p - p_L} \right) = -\ln \left(\frac{\theta}{2} \right), \quad (1.6)$$

where θ is an emission angle $\cos \theta = p_L/p$.

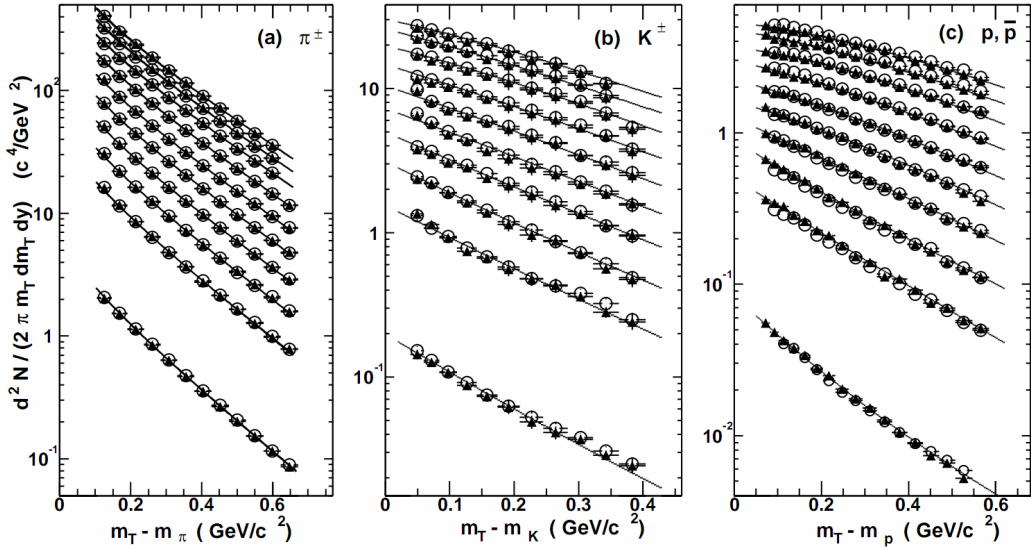


Figure 1.11: Invariant yield of particles versus transverse mass $m_T = \sqrt{p_T^2 + m_0^2}$ for π^\pm , K^\pm , p and \bar{p} at mid-rapidity for p+p collisions (bottom) and Au+Au events from 70-80% (second bottom) to 0-5% (top) centrality [14].

412
 413 The hydrodynamical expansion of a system gives the same flow velocity kick
 414 for different kind of particles - ones with bigger masses will gain larger p_T boost.
 415 This causes increase of the yield of particles with larger transverse momenta. In
 416 the invariant yield plots one can observe the decrease of the slope parameter,
 417 especially for the heavier hadrons. This is presented in the Fig. 1.11. The most
 418 affected spectra are ones of kaons (b) and protons (c). One can notice decrease
 419 of the slope parameter for heavy ion collisions (plots from second bottom to top)
 420 comparing to the proton-proton collisions (bottom ones), where no boost from
 421 radial flow should occur [8].

422 Direct photons

423 The direct photons are photons, which are not coming from the final state
 424 hadrons decays. Their sources can be various interaction from charged particles

425 created in the collision, either at the partonic or at the hadronic level. Direct
 426 photons are considered to be an excellent probe of the early stage of the collision.
 427 This is because their mean free path is very large to the created system in the
 428 collision. Thus photons created at the early stage leave the system without suf-
 429 fering any interaction and retain information about this stage, in particular about
 430 its temperature.

431 One can distinguish two kinds of direct photons: *thermal* and *prompt*. Thermal
 432 photons can be emitted from the strong processes in the quark-gluon plasma in-
 433 volving quarks and gluons or hot hadronic matter (e.g. processes: $\pi\pi \rightarrow \rho\gamma$,
 434 $\pi\rho \rightarrow \pi\gamma$). Thermal photons can be observed in the low p_T region. Prompt
 435 photons are believed to come from “hard” collisions of initial state partons be-
 436 longing to the colliding nuclei. The prompt photons can be described using the
 437 pQCD. They will dominate the high p_T region. The analysis of transverse mo-
 438 mentum of spectra of direct photons revealed, that the temperature of the source
 439 of thermal photons produced in heavy ion collisions at RHIC is in the range 300-
 440 600 MeV (Fig. 1.12). Hence the direct photons had to come from a system whose
 temperature is far above from the critical temperature for QGP creation.

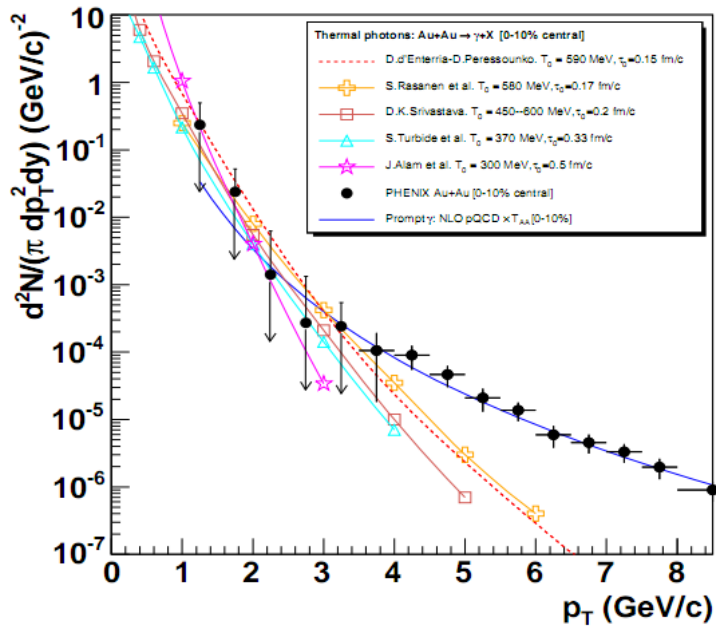


Figure 1.12: Thermal photons spectra for the central Au+Au collisions at $\sqrt{s_{NN}} = 200 \text{ GeV}$ at computed within different hydrodynamical models compared with the pQCD calculations (solid line) and experimental data from PHENIX (black dots) [15].

442 **Puzzle in di-lepton mass spectrum**

443 The invariant mass spectra (Fig. 1.13) of lepton pairs reveal many peaks cor-
 444 responding to direct decays of various mesons into a lepton pair. The continu-
 445 ous background in this plot is caused by the decays of hadrons into more than
 446 two leptons (including so-called *Dalitz decays* into a lepton pair and a photon).
 Particular hadron decay channels, which contribute to this spectrum are shown

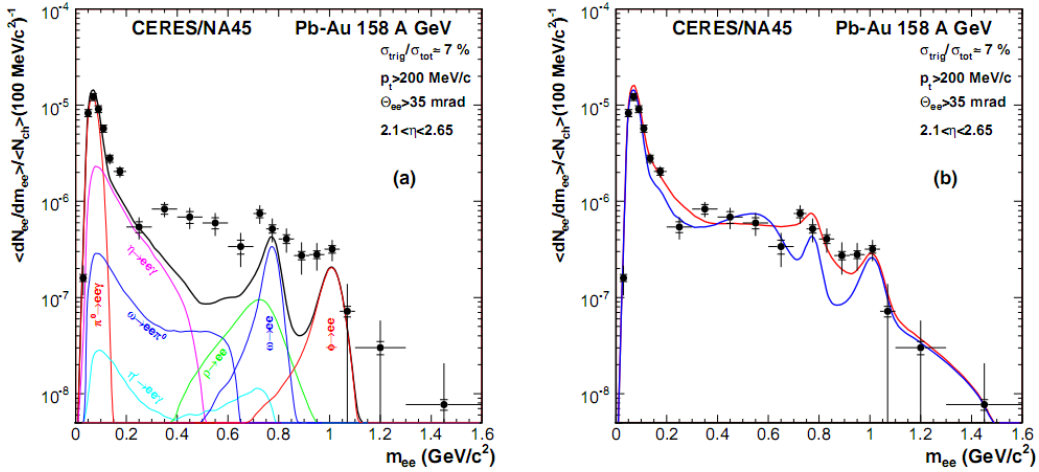


Figure 1.13: Left: Invariant mass spectrum of $e^+ - e^-$ pairs in $\text{Pb} + \text{Au}$ collisions at 158A GeV compared to the sum coming from the hadron decays predictions. Right: The expectations coming from model calculations assuming a dropping of the ρ mass (blue) or a spread of the ρ width in the medium (red) [16].

447 in the Fig. 1.13 with the coloured lines and their sum with the black one. The
 448 sum (called *the hadronic cocktail*) of various components describes experimen-
 449 tal spectra coming from the simple collisions (like $p + p$ or $p + A$) quite well with the
 450 statistical and systematical uncertainties [9]. This situation is different consider-
 451 ing more complicated systems i.e. $A + A$. Spectra coming from $\text{Pb} + \text{Au}$ collisions
 452 are presented on the plots in the Fig. 1.13. The “hadronic cocktail” does not de-
 453 scribe the data, in the mass range between the π and the ρ mesons a significant
 454 excess of electron pairs over the calculated sum is observed. Theoretical expla-
 455 nation of this phenomenon assumes modification of the spectral shape of vector
 456 mesons in a dense medium. Two different interpretations of this increase were
 457 proposed: a decrease of meson mass with the medium density and increase of the
 458 meson width in the dense medium. In principle, one could think of simultaneous
 459 occurrence of both effects: mass shift and resonance broadening. Experimental
 460 results coming from the CERES disfavour the mass shift hypothesis indicating
 461 only broadening of resonance peaks (Fig. 1.13b) [9].

463 **Jet quenching**

464 A jet is defined as a group of particles with close vector momenta and high en-
 465 ergies. It has its beginning when the two partons are going in opposite directions
 466 and have energy big enough to produce new quark-antiquark pair and then ra-
 467 diate gluons. This process can be repeated many times and it results in two back-
 468 to-back jets of hadrons. It has been found that jets in the opposite hemisphere
 469 (*away-side jets*) show a very different pattern in d+Au and Au+Au collisions. This
 470 is shown in the azimuthal correlations in the Fig. 1.14. In d+Au collisions, like in
 471 p+p, a pronounced away-side jet appears around $\Delta\phi = \pi$, exactly opposite to the
 472 trigger jet, what is typical for di-jet events. In central Au+Au collisions the away-
 jet is suppressed. When the jet has its beginning near the surface of the quark-

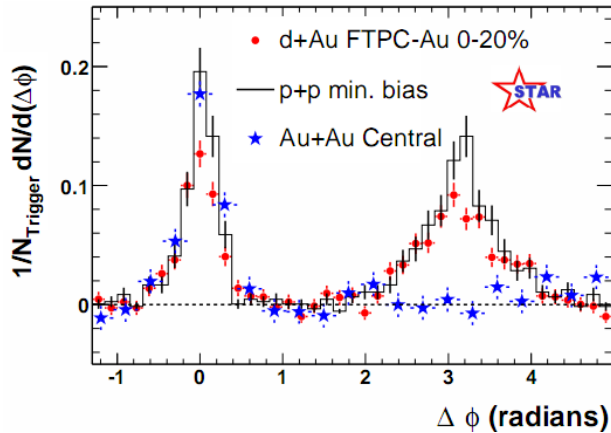


Figure 1.14: Azimuthal angle difference $\Delta\phi$ distributions for different colliding systems at $\sqrt{s_{NN}} = 200$ GeV. Transverse momentum cut: $p_T > 2$ GeV. For the Au+Au collisions the away-side jet is missing [17].

473 gluon plasma, one of the jets (*near-side jet*) leaves the system almost without any
 474 interactions. This jet is visible on the correlation plot as a high peak at $\Delta\phi = 0$.
 475 However, the jet moving towards the opposite direction has to penetrate a dense
 476 medium. The interaction with the plasma causes energy dissipation of particles
 477 and is visible on an azimuthal correlation plot as disappearance of the away-side
 478 jet [9].

480 **Chapter 2**

481 **Therminator model**

482 THERMINATOR [18] is a Monte Carlo event generator designed to investigate
483 the particle production in the relativistic heavy ion collisions. The functionality
484 of the code includes a generation of the stable particles and unstable resonances
485 at the chosen hypersurface model. It performs the statistical hadronization which
486 is followed by space-time evolution of particles and the decay of resonances. The
487 key element of this method is an inclusion of a complete list of hadronic reso-
488 nances, which contribute very significantly to the observables. The second version
489 of THERMINATOR [19] comes with a possibility to incorporate any shape of freeze-
490 out hypersurface and the expansion velocity field, especially those generated ex-
491 ternally with various hydrodynamic codes.

492 **2.1 (3+1)-dimensional viscous hydrodynamics**

493 Most of the relativistic viscous hydrodynamic calculations are done in
494 (2+1)-dimensions. Such simplification assumes boost-invariance of a matter
495 created in a collision. Experimental data reveals that no boost-invariant region is
496 formed in the collisions [20]. Hence, for the better description of created system
497 a (3+1)-dimensional model is required.

498 In the four dimensional relativistic dynamics one can describe a system
499 using a space-time four-vector $x^\nu = (ct, x, y, z)$, a velocity four-vector
500 $u^\nu = \gamma(c, v_x, v_y, v_z)$ and a energy-momentum tensor $T^{\mu\nu}$. The particular
501 components of $T^{\mu\nu}$ have a following meaning:

- 502 • T^{00} - an energy density,
- 503 • $cT^{0\alpha}$ - an energy flux across a surface x^α ,
- 504 • $T^{\alpha 0}$ - an α -momentum flux across a surface x^α multiplied by c ,
- 505 • $T^{\alpha\beta}$ - components of momentum flux density tensor,

506 where $\gamma = (1 - v^2/c^2)^{-1/2}$ is Lorentz factor and $\alpha, \beta \in \{1, 2, 3\}$. Using u^ν one can
 507 express $T^{\mu\nu}$ as follows [21]:

$$T_0^{\mu\nu} = (e + p)u^\mu u^\nu - pg^{\mu\nu} \quad (2.1)$$

508 where e is an energy density, p is a pressure and $g^{\mu\nu}$ is an inverse metric tensor:

$$g^{\mu\nu} = \begin{bmatrix} 1 & 0 & 0 & 0 \\ 0 & -1 & 0 & 0 \\ 0 & 0 & -1 & 0 \\ 0 & 0 & 0 & -1 \end{bmatrix}. \quad (2.2)$$

509 The presented version of energy-momentum tensor (Eq. 2.1) can be used to de-
 510 scribe dynamics of a perfect fluid. To take into account influence of viscosity,
 511 one has to apply the following corrections coming from shear $\pi^{\mu\nu}$ and bulk Π
 512 viscosities [22]:

$$T^{\mu\nu} = T_0^{\mu\nu} + \pi^{\mu\nu} + \Pi(g^{\mu\nu} - u^\mu u^\nu). \quad (2.3)$$

513 The stress tensor $\pi^{\mu\nu}$ and the bulk viscosity Π are solutions of dynamical equa-
 514 tions in the second order viscous hydrodynamic framework [21]. The compari-
 515 son of hydrodynamics calculations with the experimental results reveal, that the
 516 shear viscosity divided by entropy η/s has to be small and close to the AdS/CFT
 517 estimate $\eta/s = 0.08$ [22, 23]. The bulk viscosity over entropy value used in calcu-
 518 lations is $\zeta/s = 0.04$ [22].

519 When using $T^{\mu\nu}$ to describe system evolving close to local thermodynamic
 520 equilibrium, relativistic hydrodynamic equations in a form of:

$$\partial_\mu T^{\mu\nu} = 0 \quad (2.4)$$

521 can be used to describe the dynamics of the local energy density, pressure and
 522 flow velocity.

523 Hydrodynamic calculations are starting from the Glauber¹ model initial con-
 524 ditions. The collective expansion of a fluid ends at the freeze-out hypersurface.
 525 That surface is usually defined as a constant temperature surface, or equivalently
 526 as a cut-off in local energy density. The freeze-out is assumed to occur at the
 527 temperature $T = 140$ MeV.

528 2.2 Statistical hadronization

529 Statistical description of heavy ion collision has been successfully used
 530 to describe quantitatively *soft* physics, i.e. the regime with the transverse
 531 momentum not exceeding 2 GeV. The basic assumption of the statistical
 532 approach of evolution of the quark-gluon plasma is that at some point of the

¹The Glauber Model is used to calculate “geometrical” parameters of a collision like an impact parameter, number of participating nucleons or number of binary collisions.

space-time evolution of the fireball, the thermal equilibrium is reached. When the system is in the thermal equilibrium the local phase-space densities of particles follow the Fermi-Dirac or Bose-Einstein statistical distributions. At the end of the plasma expansion, the freeze-out occurs. The freeze-out model incorporated in the THERMINATOR model assumes, that chemical and thermal freeze-out occur at the same time.

2.2.1 Cooper-Frye formalism

The result of the hydrodynamic calculations is the freeze-out hypersurface Σ^μ . A three-dimensional element of the surface is defined as [19]

$$d\Sigma_\mu = \epsilon_{\mu\alpha\beta\gamma} \frac{\partial x^\alpha}{\partial \alpha} \frac{\partial x^\beta}{\partial \beta} \frac{\partial x^\gamma}{\partial \gamma} d\alpha d\beta d\gamma, \quad (2.5)$$

where $\epsilon_{\mu\alpha\beta\gamma}$ is the Levi-Civita tensor and the variables $\alpha, \beta, \gamma \in \{1, 2, 3\}$ are used to parametrize the three-dimensional freeze-out hypersurface in the Minkowski four-dimensional space. The Levi-Civita tensor is equal to 1 when the indices form an even permutation (eg. ϵ_{0123}), to -1 when the permutation is odd (e.g. ϵ_{2134}) and has a value of 0 if any index is repeated. Therefore [19],

$$d\Sigma_0 = \begin{vmatrix} \frac{\partial x}{\partial \alpha} & \frac{\partial x}{\partial \beta} & \frac{\partial x}{\partial \gamma} \\ \frac{\partial y}{\partial \alpha} & \frac{\partial y}{\partial \beta} & \frac{\partial y}{\partial \gamma} \\ \frac{\partial z}{\partial \alpha} & \frac{\partial z}{\partial \beta} & \frac{\partial z}{\partial \gamma} \end{vmatrix} d\alpha d\beta d\gamma \quad (2.6)$$

and the remaining components are obtained by cyclic permutations of t, x, y and z .

One can obtain the number of hadrons produced on the hypersurface Σ^μ from the Cooper-Frye formalism. The following integral yields the total number of created particles [19]:

$$N = (2s + 1) \int \frac{d^3 p}{(2\pi)^3 E_p} \int d\Sigma_\mu p^\mu f(p_\mu u^\mu), \quad (2.7)$$

where $f(p_\mu u^\mu)$ is the phase-space distribution of particles (for stable ones and resonances). One can simply derive from Eq. 2.7, the dependence of the momentum density [24]:

$$E \frac{d^3 N}{dp^3} = \int d\Sigma_\mu f(p_\mu u^\mu) p^\mu. \quad (2.8)$$

The momentum distribution f contains non-equilibrium corrections:

$$f = f_0 + \delta f_{shear} + \delta f_{bulk}, \quad (2.9)$$

where

$$f_0(p_\mu u^\mu) = \left\{ \exp \left[\frac{p_\mu u^\mu - (B\mu_B + I_3\mu_{I_3} + S\mu_S + C\mu_C)}{T} \right] \pm 1 \right\}^{-1} \quad (2.10)$$

558 In case of fermions, in the Eq. 2.10 there is a plus sign and for bosons, minus
 559 sign respectively. The thermodynamic quantities appearing in the $f_0(\cdot)$ are T -
 560 temperature, μ_B - baryon chemical potential, μ_{I_3} - isospin chemical potential, μ_S
 561 - strange chemical potential, μ_C - charmed chemical potential and the s is a spin of
 562 a particle. The hydrodynamic calculations yield the flow velocity at freeze-out as
 563 well as the stress and bulk viscosity tensors required to calculate non-equilibrium
 564 corrections to the momentum distribution used in Eq. 2.7. The term coming from
 565 shear viscosity has a form [22]

$$\delta f_{shear} = f_0(1 \pm f_0) \frac{1}{2T^2(e + p)} p^\mu p^\nu \pi_{\mu\nu} \quad (2.11)$$

566 and bulk viscosity

$$\delta f_{bulk} = C f_0(1 \pm f_0) \left(\frac{(u^\mu p_\mu)^2}{3u^\mu p_\mu} - c_s^2 u^\mu p_\mu \right) \Pi \quad (2.12)$$

567 where c_s is sound velocity and

$$\frac{1}{C} = \frac{1}{3} \frac{1}{(2\pi)^3} \sum_{hadrons} \int d^3p \frac{m^2}{E} f_0(1 \pm f_0) \left(\frac{p^2}{3E} - c_s^2 E \right). \quad (2.13)$$

568 The equations presented above are directly used in the THERMINATOR to gen-
 569 erate the primordial hadrons (created during freeze-out) with the Monte-Carlo
 570 method. Resonances produced in this way, propagate and decay, in cascades if
 571 necessary. For every generated particle, its origin point either on a hypersurface
 572 or is associated with the point of the decay of the parent particle. This informa-
 573 tion is kept in the simulation due to its importance for the femtoscopic analysis.

574 **Chapter 3**

575 **Particle interferometry**

576 Two-particle interferometry (also called *femtoscopy*) gives a possibility to
577 investigate space-time characteristics of the particle-emitting source created
578 in heavy ion collisions. Through the study of particle correlations, their
579 momentum distributions can be used to obtain information about the spatial
580 extent of the created system. Using this method, one can measure sizes of the
581 order of 10^{-15} m and time of the order of 10^{-23} s.

582 **3.1 HBT interferometry**

583 In the 1956 Robert Hanbury Brown and Richard Q. Twiss proposed a
584 method which through analysis of interference between photons allowed to
585 investigate angular dimensions of stars. The most important result from the
586 Hanbury-Brown-Twiss experiments is that two indistinguishable particles can
587 produce an interference effect. There is almost no difference between normal
588 interferometry and HBT method, except that the latter one does not take into account
589 information about phase shift of registered particles. At the beginning
590 this method was used in astronomy for photon interference, but this effect can
591 be used also to measure extent of any emitting source. This method was adapted
592 to heavy ion collisions to investigate dimensions of a system created in those
593 collisions by studying correlations of identical particles [25]. The main difference
594 between HBT method in astronomy and femtoscopy is that the first one is based
595 on space-time HBT correlations and the latter one uses momentum correlations.
596 The momentum correlations yield the space-time picture of the source, whereas
597 the space-time HBT correlations provide the characteristic relative momenta of
598 emitted photons, which gives the angular size of the star without the knowledge
599 of its radius and lifetime [10].

600 3.2 Theoretical approach

601 Intensity interferometry in heavy ion physics uses similar mathematical form-
 602 alism as the astronomy HBT measurement. Through the measurement of corre-
 603 lation between particles as a function of their relative momentum one can deduce
 604 the average separation between emitting sources.

605 3.2.1 Conventions used

606 In heavy ion collisions to describe particular directions, components of mo-
 607 mentum and location of particles, one uses naming convention called the Bertsch-
 Pratt coordinate system. This system is presented in the Fig. 3.1. The three dir-

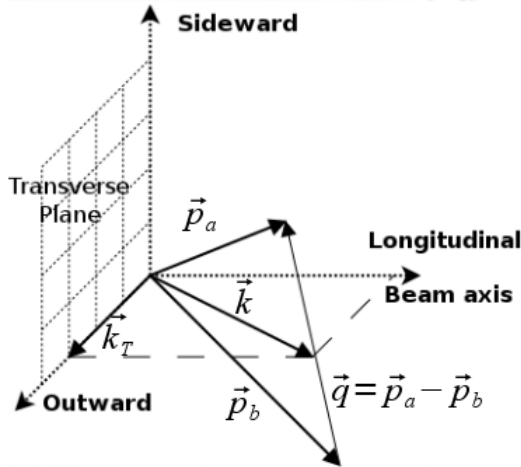


Figure 3.1: Bertsch-Pratt direction naming convention used in heavy ion collision.

608 ections are called *longitudinal*, *outward* and *sideward*. The longitudinal direction
 609 is parallel to the beam axis. The plane perpendicular to the beam axis is called
 610 a *transverse plane*. A projection of a particle pair momentum $\mathbf{k} = (\mathbf{p}_a + \mathbf{p}_b)/2$
 611 on a transverse plane (a *transverse momentum* \mathbf{k}_T) determines *outward* direction:
 612 $(\mathbf{k})_{out} = \mathbf{k}_T$. A direction perpendicular to the longitudinal and outward is called
 613 *sideward*.

614 A particle pair is usually described using two coordinate systems. The first
 615 one, *Longitudinally Co-Moving System* (**LCMS**) is moving along the particle pair
 616 with the longitudinal direction, in other words, the pair longitudinal momentum
 617 vanishes: $(\mathbf{p}_a)_{long} = -(\mathbf{p}_b)_{long}$. The second system is called *Pair Rest Frame* (**PRF**).
 618 In the PRF the centre of mass rests: $\mathbf{p}_a = -\mathbf{p}_b$. Variables which are expressed in
 619 the PRF are marked with a star (e.g. \mathbf{k}^*).

620 The transition of space-time coordinates from LCMS to PRF is simply
 a boost along the outward direction, with the transverse velocity of the

pair $\beta_T = (\mathbf{v}/c)_{out}$ [25]:

$$r_{out}^* = \gamma_t(r_{out} - \beta_T \Delta t) \quad (3.1)$$

$$r_{side}^* = r_{side} \quad (3.2)$$

$$r_{long}^* = r_{long} \quad (3.3)$$

$$\Delta t^* = \gamma_T(\Delta t - \beta_T r_{out}) , \quad (3.4)$$

where $\gamma_T = (1 - \beta_T^2)^{-1/2}$ is the Lorentz factor. However, in calculations performed in this work the equal time approximation is used, which assumes that particles in a pair were produced at the same time in PRF - the Δt^* is neglected.

The most important variables used to describe particle pair are their total momentum $\mathbf{P} = \mathbf{p}_a + \mathbf{p}_b$ and relative momentum $\mathbf{q} = \mathbf{p}_a - \mathbf{p}_b$. In the PRF one has $\mathbf{q} = 2\mathbf{k}^*$, where \mathbf{k}^* is a momentum of the first particle in PRF.

3.2.2 Two particle wave function

Let us consider two identical particles with momenta \mathbf{p}_1 and \mathbf{p}_2 emitted from space points \mathbf{x}_1 and \mathbf{x}_2 . Those emitted particles can be treated as two incoherent waves. If the particles are identical, they are also indistinguishable, therefore one

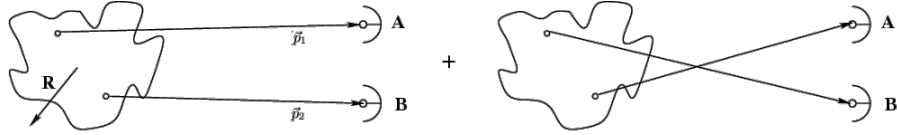


Figure 3.2: The pair wave function is a superposition of all possible states. In case of particle interferometry it includes two cases: particles with momenta p_1, p_2 registered by detectors A, B and p_1, p_2 registered by B, A respectively.

has also take into account the scenario, where the particle with momentum \mathbf{p}_1 is emitted from \mathbf{x}_2 and particle \mathbf{p}_2 from \mathbf{x}_1 (Fig. 3.2). In such case, the wave function describing behaviour of a pair has to contain both components [8]:

$$\Psi_{ab}(\mathbf{q}) = \frac{1}{\sqrt{2}} [\exp(-i\mathbf{p}_1\mathbf{x}_1 - i\mathbf{p}_2\mathbf{x}_2) \pm \exp(-i\mathbf{p}_2\mathbf{x}_1 - i\mathbf{p}_1\mathbf{x}_2)] . \quad (3.5)$$

A two particle wave function of identical bosons is symmetric ("+" sign in Eq. 3.5) and in case of identical fermions - antisymmetric ("−" sign). This anti-symmetrization or symmetrization implies the correlation effect coming from the Fermi-Dirac or Bose-Einstein statistics accordingly.

To provide full description of a system consisting of two charged hadrons, one has to include in the wave function besides quantum statistics also Coulomb and strong Final State Interactions. Considering identical particles systems, the quantum statistics is a main source of a correlation. Hence, in case of space-time analysis of particle emitting source, effects coming from the Coulomb and Strong interactions can be neglected.

3.2.3 Source emission function

To describe particle emitting source, one uses a single emission function [25]:

$$S_A(\mathbf{x}_1, \mathbf{p}_1) = \int S(\mathbf{x}_1, \mathbf{p}_1, \mathbf{x}_2, \mathbf{p}_2, \dots, \mathbf{x}_N, \mathbf{p}_N) d\mathbf{x}_2 d\mathbf{p}_2 \dots d\mathbf{x}_N d\mathbf{p}_N \quad (3.6)$$

and a two-particle one:

$$S_{AB}(\mathbf{x}_1, \mathbf{p}_1, \mathbf{x}_2, \mathbf{p}_2) = \int S(\mathbf{x}_1, \mathbf{p}_1, \mathbf{x}_2, \mathbf{p}_2, \dots, \mathbf{x}_N, \mathbf{p}_N) d\mathbf{x}_3 d\mathbf{p}_3 \dots d\mathbf{x}_N d\mathbf{p}_N . \quad (3.7)$$

Emission function $S(\cdot)$ can be interpreted as a probability to emit a particle, or a pair of particles from a given space-time point with a given momentum. In principle, the source emission function should encode all physics aspects of the particle emission process i.e. the symmetrization for bosons and fermions, as well as the two-body and many body Final State Interactions. Instead of this, one assume that each particle's emission process is independent - the interaction between final-state particles after their creation is independent from their emission process. The assumption of this independence allows to construct two-particle emission function from single particle emission functions via a convolution [25]:

$$S(\mathbf{k}^*, \mathbf{r}^*) = \int S_A(\mathbf{p}_1, \mathbf{x}_1) S_B(\mathbf{p}_2, \mathbf{x}_2) \delta \left[\mathbf{k}^* - \frac{\mathbf{p}_1 + \mathbf{p}_2}{2} \right] \delta [\mathbf{r}^* - (\mathbf{x}_1 + \mathbf{x}_2)] \times d^4 \mathbf{x}_1 d^4 \mathbf{x}_2 d^4 \mathbf{x}_1 d^3 \mathbf{p}_1 d^3 \mathbf{p}_2 \quad (3.8)$$

In case of identical particles, ($S_A = S_B$) several simplifications can be made. A convolution of the two same Gaussian distributions is also a Gaussian distribution with σ multiplied by $\sqrt{2}$. Femtoscopy can give information only about two-particle emission function, but when considering Gaussian distribution as a source function in Eq. 3.8, one can obtain a σ of a single emission function from a two-particle emission function. The Eq. 3.8 is not reversible - an information about $S_A(\cdot)$ cannot be derived from $S_{AB}(\cdot)$. An exception from this rule is a Gaussian source function, hence it is often used in femtoscopic calculations. Considering pairs of identical particles, an emission function is assumed to be described by the following equation in the Pair Rest Frame [25]:

$$S_{1D}^{PRF}(\mathbf{r}^*) = \exp \left(-\frac{r_{out}^{*2} + r_{side}^{*2} + r_{long}^{*2}}{4R_{inv}^2} \right) . \quad (3.9)$$

To change from the three-dimensional variables to the one-dimensional variable one requires introduction of the proper Jacobian r^{*2} .

$$S_{1D}^{PRF}(r^*) = r^{*2} \exp \left(-\frac{r^{*2}}{4R_{inv}^2} \right) . \quad (3.10)$$

668 The “4” in the denominator before the “standard deviation” R_{inv} in the Gaussian
 669 distribution comes from the convolution of the two Gaussian distributions,
 670 which multiplies the R_{inv} by a factor of $\sqrt{2}$.

A more complex form of emission function was used by all RHIC and SPS experiments in identical pion femtoscopy:

$$S_{3D}^{LCMS}(\mathbf{r}) = \exp \left(-\frac{r_{out}^2}{4R_{out}^2} - \frac{r_{side}^2}{4R_{side}^2} - \frac{r_{long}^2}{4R_{long}^2} \right). \quad (3.11)$$

671 The main difference of this source function is that it has three different and inde-
 672 pendent widths R_{out} , R_{side} , R_{long} and they are defined in the LCMS, not in PRF.
 673 Unlike in PRF, in LCMS an equal-time approximation is not used. For identical
 674 particles this is not a problem - only Coulomb interaction inside a wave function
 675 depends on Δt .

676 Relationship between one-dimensional and three-dimensional source sizes

677 Up to now, most of femtoscopic measurements were limited only to averaged
 678 source size R_{av}^L (the letter “L” in superscript stands for LCMS):

$$S_{1D}^{LCMS}(\mathbf{r}) = \exp \left(-\frac{r_{out}^2 + r_{side}^2 + r_{long}^2}{2R_{av}^L} \right). \quad (3.12)$$

679 The relationship between between $S_{1D}^{LCMS}(\cdot)$ and $S_{3D}^{LCMS}(\cdot)$ is given by:

$$S_{3D}^{LCMS}(r) = \int \exp \left(-\frac{r_{out}^2}{2R_{out}^L} - \frac{r_{side}^2}{2R_{side}^L} - \frac{r_{long}^2}{2R_{long}^L} \right) \times \delta \left(r - \sqrt{r_{out}^2 + r_{side}^2 + r_{long}^2} \right) dr_{out} dr_{side} dr_{long}. \quad (3.13)$$

680 The one-dimensional source size corresponding to the three-dimensional one can
 681 be approximated by the following form:

$$S_{1D}^{LCMS}(r) = r^2 \exp \left(-\frac{r^2}{2R_{av}^L} \right). \quad (3.14)$$

682 The equation above assumes that $R_{out}^L = R_{side}^L = R_{long}^L$ hence $R_{av}^L = R_{out}^L$. If this
 683 condition is not satisfied, one can not give explicit mathematical relation between
 684 one-dimensional and three-dimensional source sizes. However, for realistic val-
 685 ues of R (i.e. for similar values of R_{out} , R_{side} , R_{long}), the S_{3D}^{LCMS} from Eq. 3.13 is
 686 not very different from Gaussian distribution and can be well approximated by
 687 Eq. 3.13.

688 A deformation of an averaged source function in case of big differences in
 689 R_{out} , R_{side} , R_{long} is presented in the Fig. 3.3. A three-dimensional Gaussian dis-
 690 tribution with varying widths was averaged into one-dimensional function using

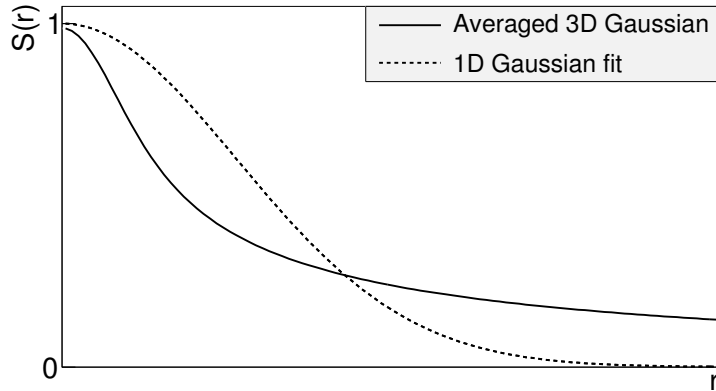


Figure 3.3: An averaged three-dimensional Gaussian source function with different widths was averaged into one-dimensional function. To illustrate deformations, one-dimensional Gaussian distribution was fitted.

the Eq. 3.13. Afterwards, an one-dimensional Gaussian distribution was fitted.
One can notice a heavy tail of an averaged distribution in long r region, which
makes an approximation using one-dimensional distribution in this case quite
inaccurate.

Using Eq. 3.13 and Eq. 3.14 one can obtain a relation between one-dimensional width and the three-dimensional ones. Through numerical calculations one can find the following approximate relation [25]:

$$R_{av}^L = \sqrt{\left(R_{out}^{L^2} + R_{side}^{L^2} + R_{long}^{L^2}\right)/3}. \quad (3.15)$$

This equation does not depend on the pair velocity, hence it is valid in the LCMS and PRF.

3.2.4 Theoretical correlation function

The fundamental object in a particle interferometry is a correlation function.
The correlation function is defined as:

$$C(\mathbf{p}_a, \mathbf{p}_b) = \frac{P_2(\mathbf{p}_a, \mathbf{p}_b)}{P_1(\mathbf{p}_a)P_1(\mathbf{p}_b)}, \quad (3.16)$$

where P_2 is a conditional probability to observe a particle with momentum \mathbf{p}_b if particle with momentum \mathbf{p}_a was also observed. A P_1 is a probability to observe a particle with a given momentum. The relationship between source emission function, pair wave function and the correlation function is described by the following equation:

$$C(\mathbf{p}_1, \mathbf{p}_2) = \int S_{AB}(\mathbf{p}_1, \mathbf{x}_1, \mathbf{p}_2, \mathbf{x}_2) |\Psi_{AB}|^2 d^4\mathbf{x}_1 d^4\mathbf{x}_2 \quad (3.17)$$

Substituting the one-dimensional emission function (Eq. 3.10) into the integral above yields the following form of correlation function in PRF:

$$C(q) = 1 + \lambda \exp(-R_{inv}^2 q^2) \quad (3.18)$$

where q is a momentum difference between two particles. When using the three-dimensional emission function (Eq. 3.11) one gets the following correlation function defined in the LCMS:

$$C(\mathbf{q}) = 1 + \lambda \exp(-R_{out}^2 q_{out}^2 - R_{side}^2 q_{side}^2 - R_{long}^2 q_{long}^2) \quad (3.19)$$

where q_{out} , q_{side} , q_{long} are \mathbf{q} components in the outward, sideward and longitudinal direction. The λ parameter in the equations above determines correlation strength. The lambda parameter has values in the range $\lambda \in [-0.5, 1]$ and it depends on a pair type. In case of pairs of identical bosons (like $\pi\pi$ or KK) the lambda parameter $\lambda \rightarrow 1$. For identical fermions (e.g. $p-p$) $\lambda \rightarrow -0.5$. Values of λ observed experimentally are lower than 1 (for bosons) and greater than -0.5 (for fermions). There are few explanations to this effect: detector efficiencies, inclusion of misidentified particles in a used sample or inclusion of non-correlated pairs (when one or both particles come from e.g. long-lived resonance). The analysis carried out in this work uses data from a model, therefore the detector efficiency and particle purity is not taken into account [25].

3.2.5 Spherical harmonics decomposition of a correlation function

Results coming from an analysis using three-dimensional correlation function in Cartesian coordinates are quite difficult to visualize. To do that, one usually performs a projection into a one dimension in outward, sideward and longitudinal directions. One may loose important information about a correlation function in this procedure, because it gives only a limited view of the full three-dimensional structure. Recently, a more advanced way of presenting correlation function - a spherical harmonics decomposition, was proposed. The three-dimensional correlation function is decomposed into an infinite set of components in a form of one-dimensional histograms $C_l^m(q)$. In this form, a correlation function is defined as a sum of a series [26]:

$$C(\mathbf{q}) = \sum_{l,m} C_l^m(q) Y_l^m(\theta, \phi), \quad (3.20)$$

where $Y_l^m(\theta, \phi)$ is a spherical harmonic function. Spherical harmonics are an orthogonal set of solutions to the Laplace's equation in spherical coordinates. Hence, in this approach, a correlation function is defined as a function of q , θ and ϕ . To obtain C_l^m coefficients in the series, one has to calculate the following integral:

$$C_l^m(q) = \int_{\Omega} C(q, \theta, \phi) Y_l^m(\theta, \phi) d\Omega, \quad (3.21)$$

732 where Ω is a full solid angle.

Spherical harmonics representation has several important advantages. The main advantage of this decomposition is that it requires less statistics than traditional analysis performed in Cartesian coordinates. Another one is that it encodes full three-dimensional information in a set of one-dimensional plots. In principle it does not have to be an advantage, because full description of a correlation function requires infinite number of l, m components. But it so happens that the intrinsic symmetries of a pair distribution in a femtoscopic analysis result in most of the components to vanish. For the identical particles correlation functions, all coefficients with odd values of l and m disappear. It has also been shown, that the most significant portion of femtoscopic data is stored in the components with the lowest l values. It is expected that, the main femtoscopic information is contained in the following components [25]:

$$C_0^0 \rightarrow R_{LCMS}, \quad (3.22)$$

$$\Re C_2^0 \rightarrow \frac{R_T}{R_{long}}, \quad (3.23)$$

$$\Re C_2^2 \rightarrow \frac{R_{out}}{R_{side}}, \quad (3.24)$$

733 where $R_{LCMS} = \sqrt{(R_{out}^2 + R_{side}^2 + R_{long}^2)/3}$ and $R_T = \sqrt{(R_{out}^2 + R_{side}^2)/2}$.

734 The C_0^0 is sensitive to the overall size of a correlation function. The $\Re C_2^0$ carries
 735 the information about the ratio of the transverse to the longitudinal radii, due
 736 to its $\cos^2(\theta)$ weighting in Y_2^0 . The component $\Re C_2^2$ with its $\cos^2(\phi)$ weighting
 737 encodes the ratio between outward and sideward radii. Thus, the spherical har-
 738 monics method allows to obtain and analyze full three-dimensional femtoscopic
 739 information from a correlation function [25].

740 3.3 Experimental approach

741 The correlation function is defined as a probability to observe two particles
 742 together divided by the product of probabilities to observe each of them sepa-
 743 rately (Eq. 3.16). Experimentally this is achieved by dividing two distributions
 744 of relative momentum of pairs of particles coming from the same event and the
 745 equivalent distribution of pairs where each particle is taken from different colli-
 746 sions. In this way, one obtains not only femtoscopic information but also all other
 747 event-wide correlations. This method is useful for experimentalists to estimate
 748 the magnitude of non-femtoscopic effects. There exists also a different approach,
 749 where two particles in pairs in the second distribution are also taken from the
 750 same event. The second method gives only information about physical effects
 751 accessible via femtoscopy. The aim of this work is a study of effects coming from
 752 two particle interferometry, hence the latter method was used.

753 In order to calculate experimental correlation function, one uses the follow-
 754 ing approach. One has to construct two histograms: the *numerator* N and the

755 denominator D with the particle pairs momenta, where particles are coming from
 756 the same event. Those histograms can be one-dimensional (as a function of $|\mathbf{q}|$),
 757 three dimensional (a function of three components of \mathbf{q} in LCMS) or a set of one-
 758 dimensional histogram representing components of the spherical harmonic de-
 759 composition of the distribution. The second histogram, D is filled for each pair
 760 with the weight 1.0 at a corresponding relative momentum $\mathbf{q} = 2\mathbf{k}^*$. The first one,
 761 N is filled with the same procedure, but the weight is calculated as $|\Psi_{ab}(\mathbf{r}^*, \mathbf{k}^*)|^2$.
 762 A division N/D gives the correlation function C . This procedure can be simply
 763 written as [25]:

$$C(\mathbf{k}^*) = \frac{N}{D} = \frac{\sum_{n_i \in D} \delta(\mathbf{k}^*_i - \mathbf{k}^*) |\Psi_{ab}(\mathbf{r}^*_i, \mathbf{k}^*_i)|^2}{\sum_{n_i \in D} \delta(\mathbf{k}^*_i - \mathbf{k}^*)} . \quad (3.25)$$

The D histogram represents the set of all particle pairs used in calculations.
 The n_i is a pair with the its relative momentum \mathbf{k}^*_i and relative separation \mathbf{r}^*_i .
 The wave function used in Eq. 3.25 has one of the following forms:

$$|\Psi_{\pi\pi}(\mathbf{r}^*, \mathbf{k}^*)|^2 = |\Psi_{KK}(\mathbf{r}^*, \mathbf{k}^*)|^2 = 1 + \cos(2\mathbf{k}^*\mathbf{r}^*) , \quad (3.26)$$

$$|\Psi_{pp}(\mathbf{r}^*, \mathbf{k}^*)|^2 = 1 - \frac{1}{2} \cos(2\mathbf{k}^*\mathbf{r}^*) . \quad (3.27)$$

764 The first one is used in case of bosons, and the latter one is for identical fermi-
 765 ons. Mathematically, the procedure of calculating the Eq. 3.25 is equivalent to a
 766 calculation of an integral in Eq. 3.17 through a Monte-Carlo method.

767 3.4 Scaling of femtoscopic radii

768 In the hydrodynamic models describing expansion of a quark-gluon plasma,
 769 particles are emitted from the source elements. Each of the source elements is
 770 moving with the velocity u_μ given by hydrodynamic equations. Because solu-
 771 tions of those equations are smooth, nearby source elements have similar velo-
 772 cities. Each emitted particle from a certain source element is boosted with the
 773 flow velocity u_μ according to the point of origin. Hence particles emitted close
 774 to each other (pairs with large transverse momentum $|\mathbf{k}_T|$) will gain the similar
 775 velocity boost, they can combine into pairs with small relative momenta ($|\mathbf{q}|$) and
 776 therefore become correlated. If the two particles are emitted far away from each
 777 other (a pair with small $|\mathbf{k}_T|$), the flow field u_μ in their point of emission might
 778 be very different and it will be impossible for them to have sufficiently small rel-
 779 ative momenta in order to be in region of interference effect. This effect is visible
 780 in a width of a correlation function in the Fig. 3.4. The correlation function gets
 781 broader for greater values of $|\mathbf{k}_T|$ and the femtoscopic radius R becomes smal-
 782 ler [8, 27].

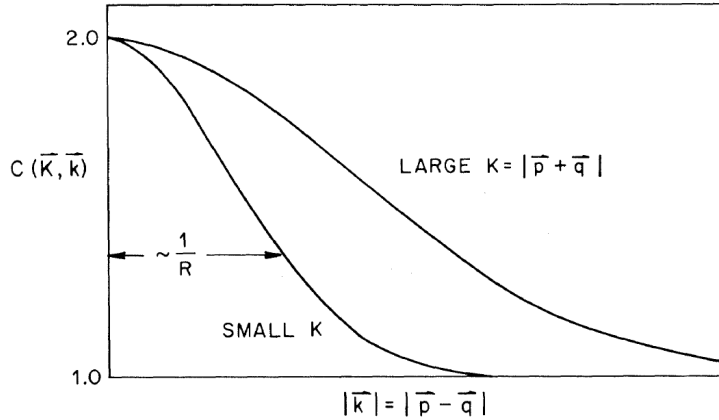


Figure 3.4: Correlation function width dependence on total pair momentum. Pion pairs with a large total momentum are more correlated [27].

783 3.4.1 Scaling in LCMS

Hydrodynamic calculations performed in LCMS show that femtoscopic radii in outward, sideward, and longitudinal direction show dependence on transverse mass $m_T = \sqrt{k_T^2 + m^2}$, where m is a mass of a particle [28]. Moreover, experimental results show that this scaling is observed for R_{LCMS} radii also. This dependence can be expressed as follows:

$$R_i = \alpha m_T^{-\beta} \quad (3.28)$$

784 where i subscript indicates that this equation applies to R_{out} , R_{side} and R_{long}
 785 radii. The β exponent is approximately equal 0.5. In case of strong transversal
 786 expansion of the emitting source, the decrease of longitudinal interferometry ra-
 787 dius can be more quick than $m_T^{-0.5}$, hence one can expect for longitudinal radii
 788 greater values of $\beta > 0.5$ [28].

789 3.4.2 Scaling in PRF

790 In the collisions at the LHC energies, pions are most abundant particles and
 791 their multiplicities are large enough to enable three-dimensional analysis. How-
 792 ever, for heavier particles, such as kaons and protons statistical limitations arise.
 793 Hence it is often possible to only measure one-dimensional radius R_{inv} for those
 794 particles. The R_{inv} is then calculated in the PRF. The transition from LCMS to
 795 PRF is a Lorentz boost in the direction of pair transverse momentum with velo-
 796 city $\beta_T = p_T/m_T$. Hence only R_{out} radius changes:

$$R_{out}^* = \gamma_T R_{out}. \quad (3.29)$$

797 The one-dimensional R_{inv} radius is direction-averaged source size in PRF. One
 798 can notice, that such power-law scaling of R_{inv} described by Eq. 3.28 is not

799 observed. To recover such scaling in PRF one has to take into consideration two
 800 effects when transforming variables from LCMS to PRF: overall radius growths
 801 and source distribution becomes non-Gaussian, while developing long-range
 802 tails (see Fig. 3.3 for an example). The interplay of these two effects can be
 803 accounted with an approximate formula:

$$R_{inv} = \sqrt{(R_{out}^2 \sqrt{\gamma_T} + R_{side}^2 + R_{long}^2)/3} . \quad (3.30)$$

Assuming that all radii are equal $R_{out} = R_{side} = R_{long}$ this formula can be simplified:

$$R_{LCMS} \approx R_{inv} \times [(\sqrt{\gamma_T} + 2)/3]^{-1/2} . \quad (3.31)$$

804 This approximate formula allows to restore power-law behaviour of the scaled
 805 radii not only when the radii are equal, but also when their differences are small
 806 (for explanation see the last part of the section 3.2.3).

807 This method of recovering scaling in PRF can be used as a tool for the search
 808 of hydrodynamic collectivity between pions, kaons and protons in heavy ion col-
 809 lisions with the measurement of one-dimensional radius in PRF.

810 **Chapter 4**

811 **Results**

812 For the purposes of the femtoscopic analysis in this thesis, the THERMINATOR
813 model was used to generate large number of events for eight different sets of
814 initial conditions corresponding the following centrality ranges: 0-5%, 0-10%, 10-
815 20%, 20-30%, 30-40%, 40-50%, 50-60% and 60-70% for the Pb-Pb collisions at the
816 centre of mass energy $\sqrt{s_{NN}} = 2.76 \text{ TeV}$.

817 **4.1 Identical particles correlations**

818 The correlation functions (three-dimensional and one-dimensional) were cal-
819 culated separately for the following different pairs of identical particles: π - π , K -
820 K and p - p for nine k_T bins (in GeV/c): 0.1-0.2, 0.2-0.3, 0.3-0.4, 0.4-0.5, 0.6-0.7,
821 0.7-0.8, 0.8-1.0 and 1.0-1.2. In case of kaons, k_T ranges start from 0.3 and for pi-
822 ons from 0.4 and for both of them the maximum value is 1.0. The k_T ranges for
823 the heavier particles were limited to maintain sufficient multiplicity to perform
824 reliable calculations.

825 **4.1.1 Spherical harmonics components**

826 The three-dimensional correlation function as a function of relative
827 momentum q_{LCMS} was calculated in a form of components of spherical
828 harmonics series accordingly to the Eq. 3.21. In the femtoscopic analysis of
829 identical particles, the most important information is stored in the $\Re C_0^0$, $\Re C_2^0$
830 and $\Re C_2^2$, hence only those components were analyzed. Correlation functions
831 obtained in this procedure were calculated for the different centrality bins for the
832 pairs of pions, kaons and protons. They are presented in the Fig. 4.1, 4.2 and 4.3.

833 Coefficients for pairs of identical bosons (pions and kaons) are shown in the
834 Fig. 4.1 and 4.2. The wave function symmetrization (Bose-Einstein statistics)
835 causes the increase of a correlation in the low relative momenta regime ($q_{LCMS} <$
836 0.06 GeV/c or even $q_{LCMS} < 0.12 \text{ GeV/c}$ for more peripheral collisions). It is
837 clearly visible in the $\Re C_0^0$ component. The $\Re C_0^0$ resembles one-dimensional cor-

relation function and in fact it encodes information about overall source radius. The second coefficient $\Re C_2^0$ differs from zero (is negative), which yields the information about the ratio R_T/R_{long} . The $\Re C_2^2$ stores the R_{out}/R_{side} ratio and one can notice that is non-vanishing (is also negative).

The correlation function for a pair of identical fermions is presented in the Fig. 4.3. An influence of wave function anti-symmetrization (Fermi-Dirac statistics) has its effect in the decrease of a correlation down to 0.5 at low relative momentum ($q_{LCMS} < 0.1 \text{ GeV/c}$ or $q_{LCMS} < 0.15 \text{ GeV/c}$ for more peripheral collisions), which can be observed in $\Re C_0^0$. The $\Re C_2^0$ and $\Re C_2^2$ coefficients differ from zero and are becoming positive.

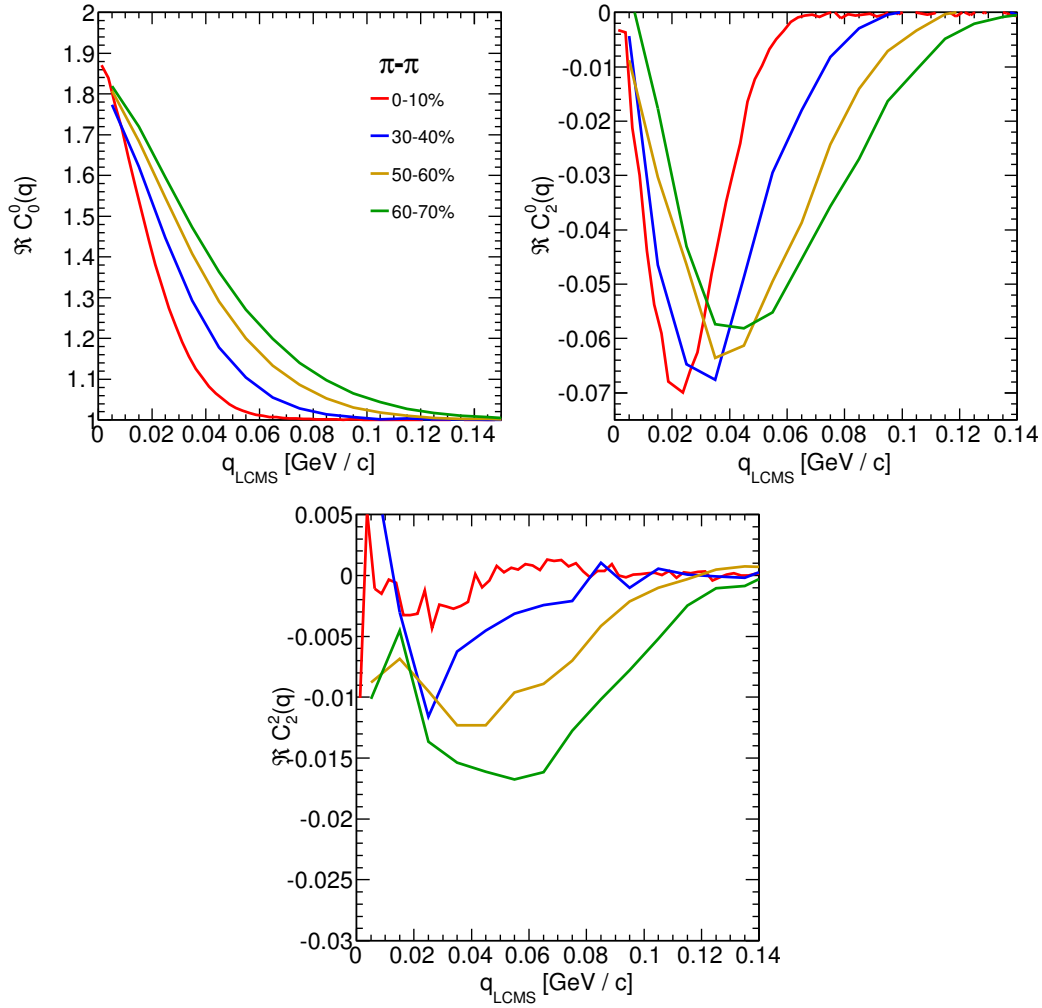


Figure 4.1: Spherical harmonics coefficients of the two-pion correlation function. From the top left: $\Re C_0^0$, $\Re C_2^0$ and $\Re C_2^2$. Only few centrality bins are presented for increased readability.

848 The common effect of the spherical harmonics form of a correlation function
 849 is the “mirroring” of the shape of the $\Re C_0^0$ coefficient - when correlation func-
 850 tion increases at low q_{LCMS} , the $\Re C_2^0$ and $\Re C_2^2$ are becoming negative and vice
 851 versa. This is quite different behaviour than in the case of correlations of non-
 852 identical particles, where the $\Re C_2^0$ still behaves in the same manner, but $\Re C_2^2$ has
 853 the opposite sign to the $\Re C_2^0$ [25].

854 In all cases, the correlation function gets wider with the peripherality of a
 855 collision i.e. the correlation function for most central collisions (0-10%) is much
 856 narrower than for the most peripheral ones (60-70%). This phenomena in clearly

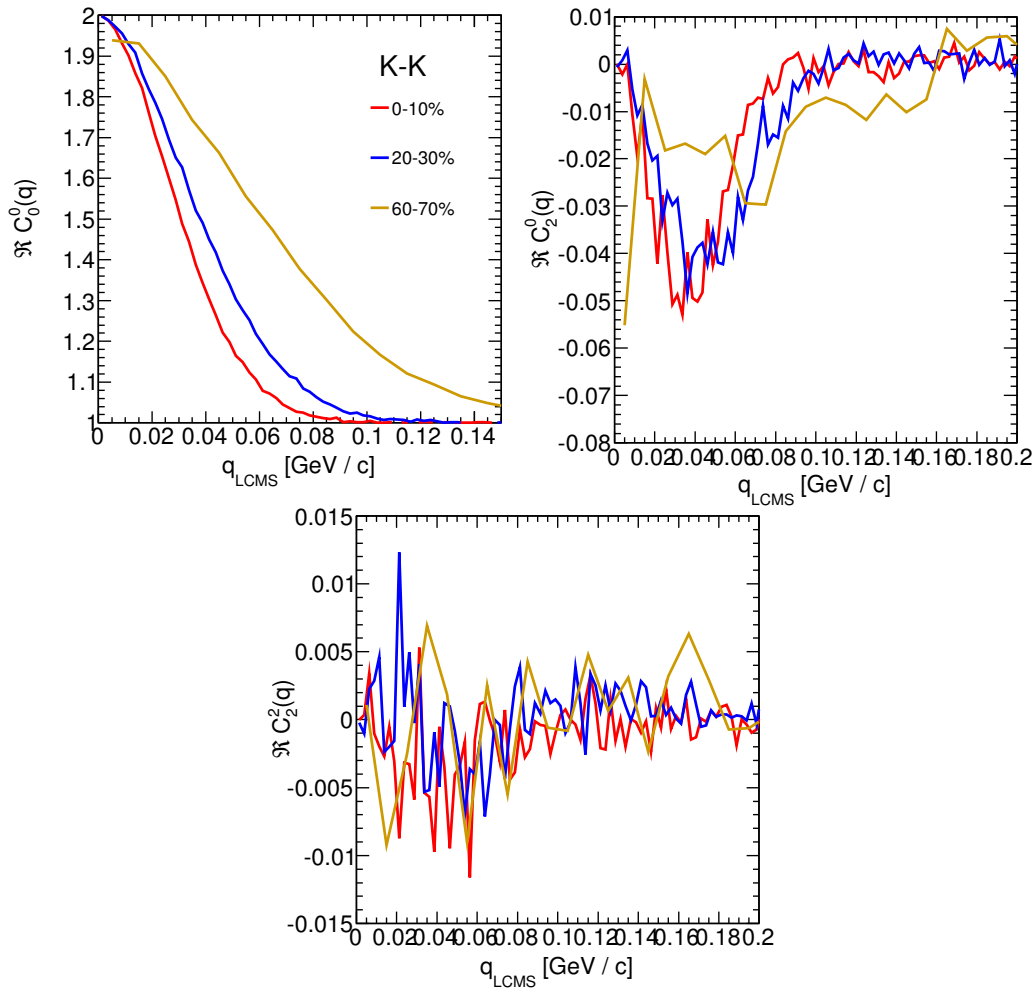


Figure 4.2: Spherical harmonics coefficients of the two-kaon correlation function. From the top left: $\Re C_0^0$, $\Re C_2^0$ and $\Re C_2^2$. Only few centrality bins are presented for increased readability. The $\Re C_2^2$ is noisy, but one can still notice that it differs from zero and is becoming negative.

visible the $\Re C_0^0$ coefficients. Other components are also affected by this effect, this is especially noticeable in the case of kaons and pions. For the protons, the results are noisy, hence this effect is not clearly distinguishable.

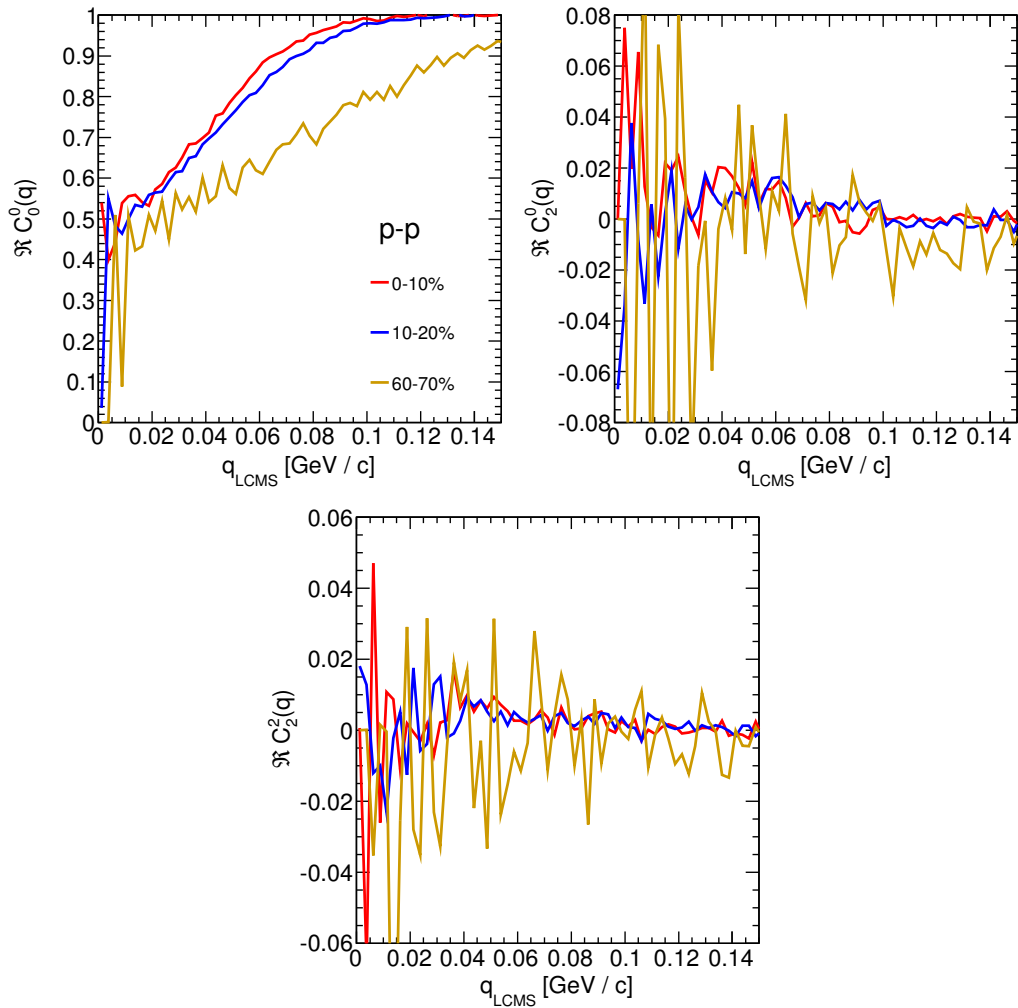


Figure 4.3: Spherical harmonics coefficients of the two-proton correlation function. From the top left: $\Re C_0^0$, $\Re C_2^0$ and $\Re C_2^2$. Only few centrality bins are presented for increased readability. The $\Re C_2^0$ and $\Re C_2^2$ are noisy, but one can still notice, that they differ from zero and are becoming positive.

860 **4.1.2 Centrality dependence of a correlation function**

861 The centrality dependence of a correlation function is especially visible in
 862 one-dimensional correlation functions. This effect is presented in the Fig. 4.4 -
 863 the correlation functions for pions, kaons and protons are plotted for the same
 864 k_T range but different centrality bins. One can notice that the width of a func-
 865 tion is smaller in the case of most central collisions. Hence, the femtoscopic radii
 866 (proportional to the inverse of width) are increasing with the centrality. An ex-
 867 planation for this growth is that in the most central collisions, a size of a created
 system is larger than for the peripheral ones.

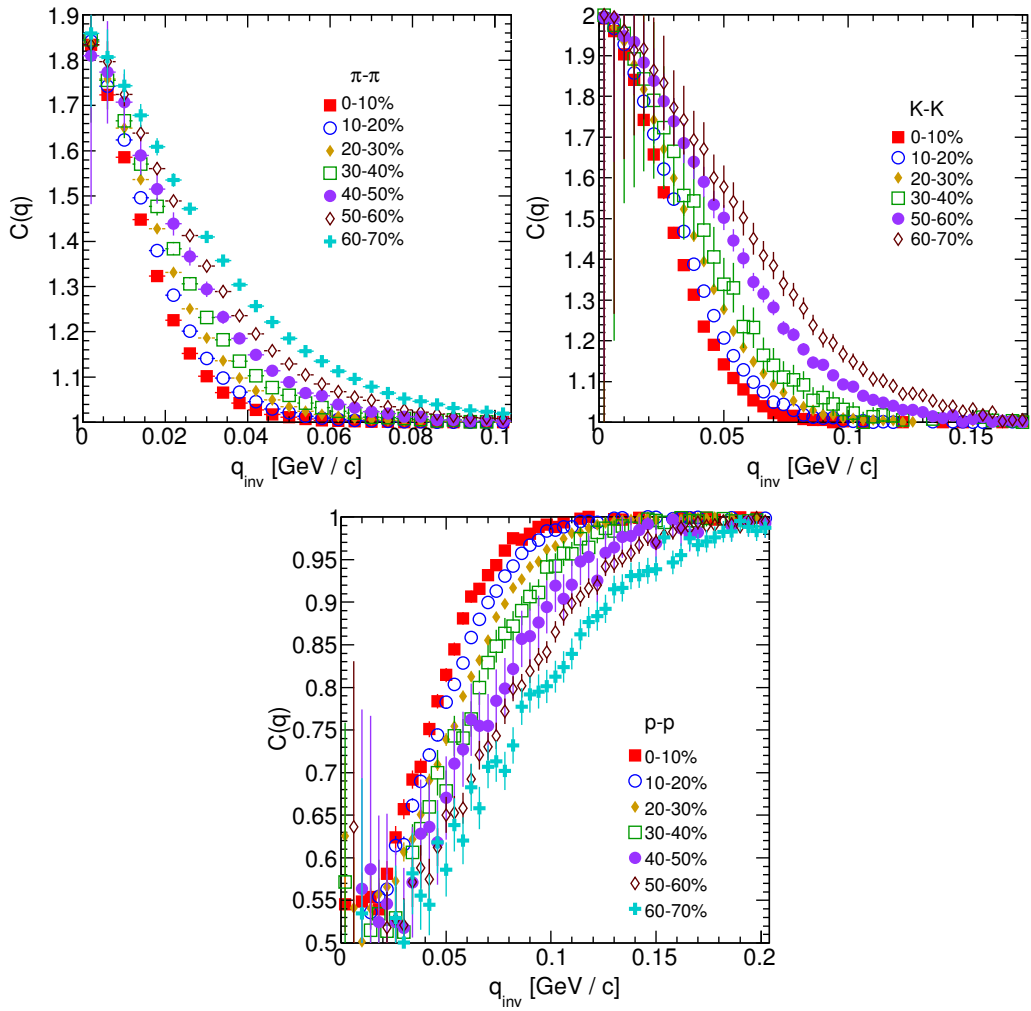


Figure 4.4: One-dimensional correlation function for pions (top left), kaons (top right) and protons (bottom) for different centralities.

869 **4.1.3 k_T dependence of a correlation function**

870 In the Fig. 4.5 there are presented one-dimensional correlation functions for
 871 pions, kaons and protons for the same centrality bin, but different k_T ranges. One
 872 can observe in all cases of the particle types, appearance of the same trend: with
 873 the increase of the total transverse momentum of a pair, the width of a correlation
 874 function increases and the femtoscopic radius decreases. The plots in the Fig. 4.5
 875 were zoomed in to show the influence of k_T .

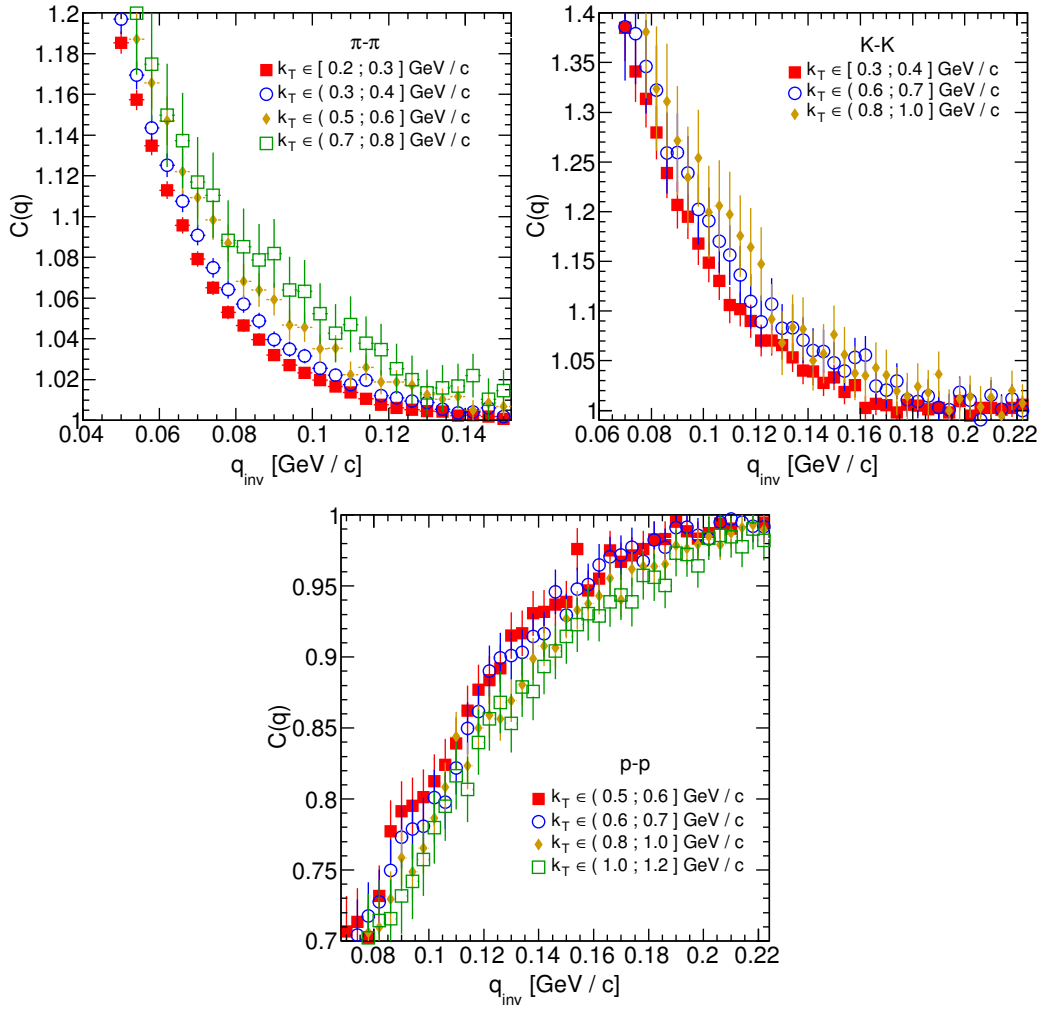


Figure 4.5: One-dimensional correlation functions for pions, kaons and protons, for the same centrality bin and different k_T ranges. The plot was zoomed in to the region which illustrates the k_T dependence in the best way. Only few of the calculated ranges are presented for better readability.

4.2 Results of the fitting procedure

In order to perform a quantitative analysis of a wide range of correlation functions, the theoretical formulas were fitted to the calculated experimental-like data. In this procedure, the femtoscopic radii for the three-dimensional as well as one-dimensional correlation functions were extracted. The main goal of this analysis is a verification of a common transverse mass scaling for different particles types. Obtained radii are plotted as a function of a transverse mass $m_T = \sqrt{k_T^2 + m^2}$. To test the scaling, the following power-law was fitted to the particular radii afterwards:

$$R_x = \alpha m_T^{-\beta}, \quad (4.1)$$

where the α and β are free parameters.

4.2.1 The three-dimensional femtoscopic radii scaling

In the Fig. 4.6 there are presented femtoscopic radii in the outward, sideward and longitudinal directions for the analysis of two-pion correlation functions in

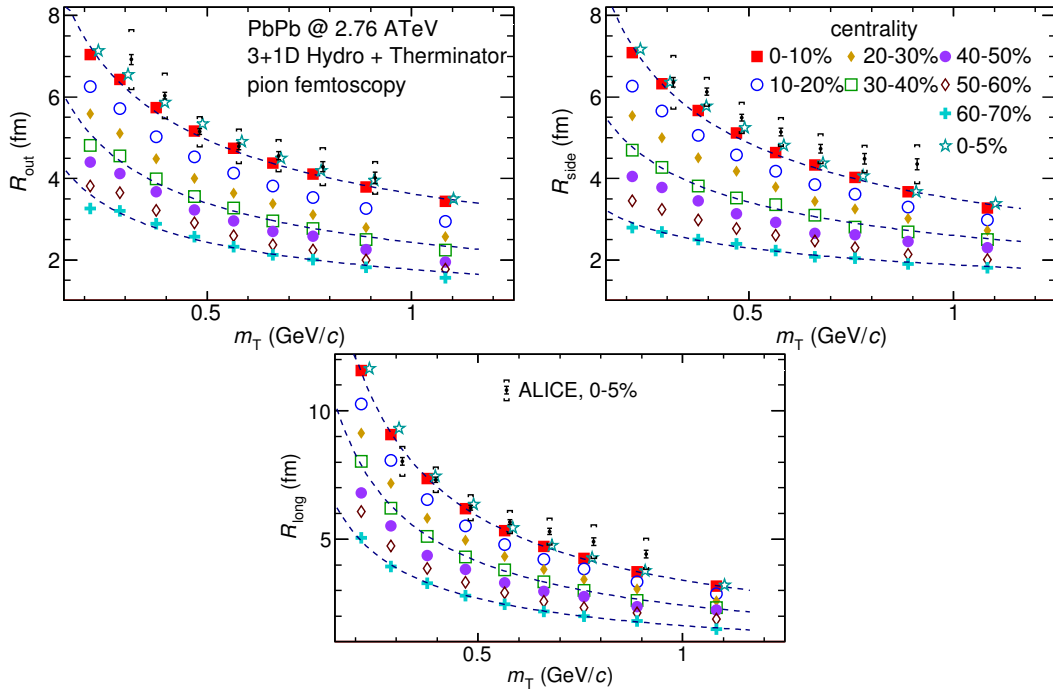


Figure 4.6: Femtoscopic radii in LCMS coming from two-pion correlation functions for all centrality bins as a function of m_T . The dashed lines are power-law fits. The most central collisions (0-5%) are compared to the results from ALICE [29]. The two datasets are shifted to the right for visibility [30].

the LCMS. The dashed lines are fits of the power law to the data. One can notice, that the power law describes well data points with a 5% accuracy. The β fit parameter for the outward direction is in the order of 0.45. For the sideward direction, this parameter has the similar value, but it is lower for the most peripheral collisions. In case of the longitudinal direction, the β has greater value, up to 0.75. In the Fig. 4.6 there are also compared results for the top 5% central collisions (star-shaped markers) with experimental data from ALICE [29]. The experimental results are consistent with the ones coming from the model predictions.

The Fig. 4.7 presents femtoscopic radii coming from the kaon calculations. The R_{out} , R_{side} and R_{long} fall also with the power-law within the 5% accuracy. The β parameter was larger in case of kaons: 0.59 in outward direction, 0.54 in the sideward and 0.86 for longitudinal.

The results for two-proton analysis are shown in the Fig. 4.8. The Eq. 4.1 was fitted to the data and tells that the protons also follow the m_T scaling within 5% range. The β parameter values were even bigger for the outward (0.58), sideward (0.61) and longitudinal (1.09) directions than for the other particle types.

The Fig. 4.9 presents results for the pions, kaons and protons together as a function of m_T . Considering differences in the β value for the fits for differ-

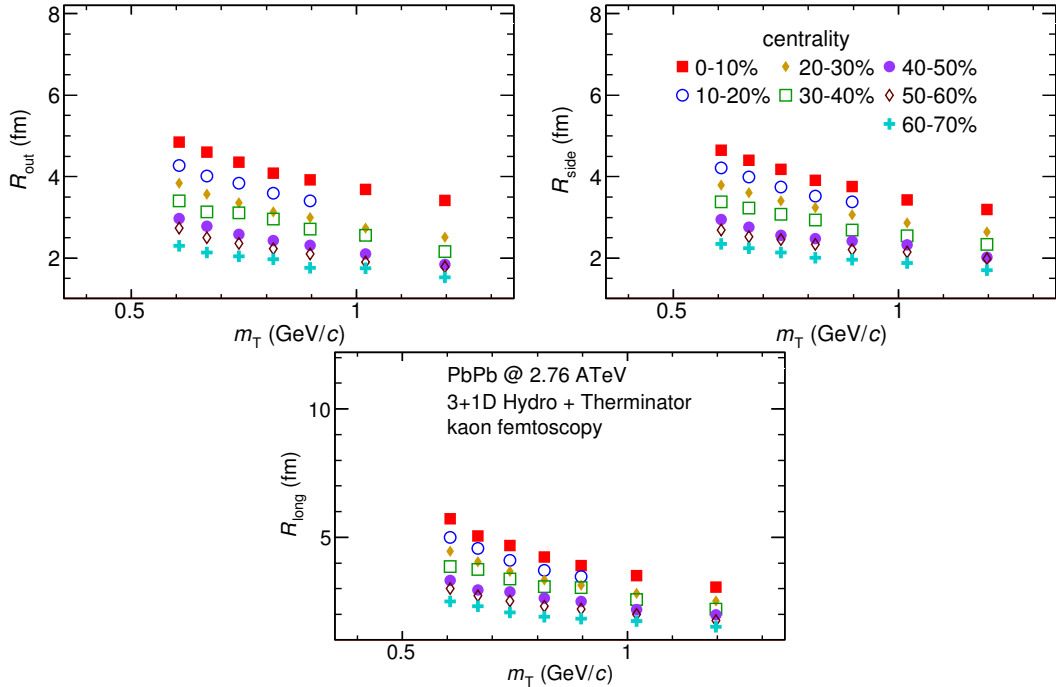


Figure 4.7: Femtoscopic radii extracted from two-kaon correlation functions for different centrality bins as a function of m_T . [30].

ent particles, one can suspect that there is no common scaling between different kinds of particles. However, when all of the results shown on the same plot, they are aligning on the common curve and the scaling is well preserved. The scaling accuracy is 3%, 5% and 4% for the 0-10%, 20-30% and 60-70% for the outward direction. For the sideward radii the scaling is better, with average deviations 2%, 2% and 3% respectively. In case of longitudinal direction the accuracy is 6%, 5% and 3% for the three centralities. The β parameter for the outward direction is close to the 0.42 in all cases. For the sideward direction it varies from 0.28 to 0.47 and is bigger for more central collisions. Regarding longitudinal radii, the exponent is bigger than the other two: $\beta \in [0.62; 0.72]$. Considering all results, the plotted radii are following the common power-law scaling within the 5% accuracy for all directions, centralities and particle types.

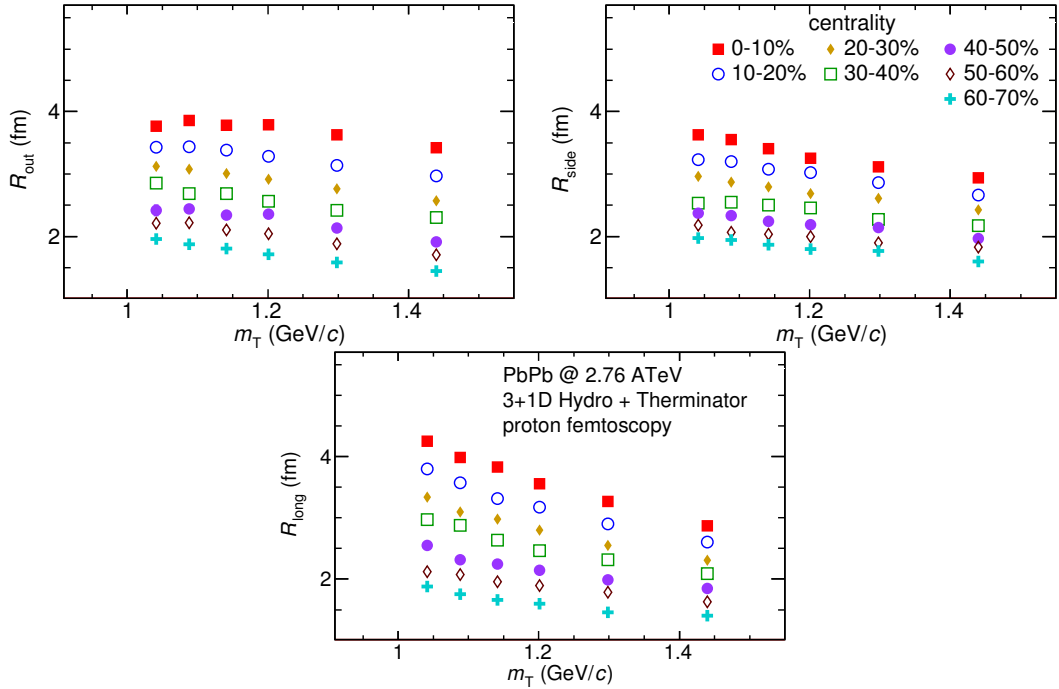


Figure 4.8: Femtoscopic radii extracted from two-proton correlation functions for different centrality bins as a function of m_T . [30].

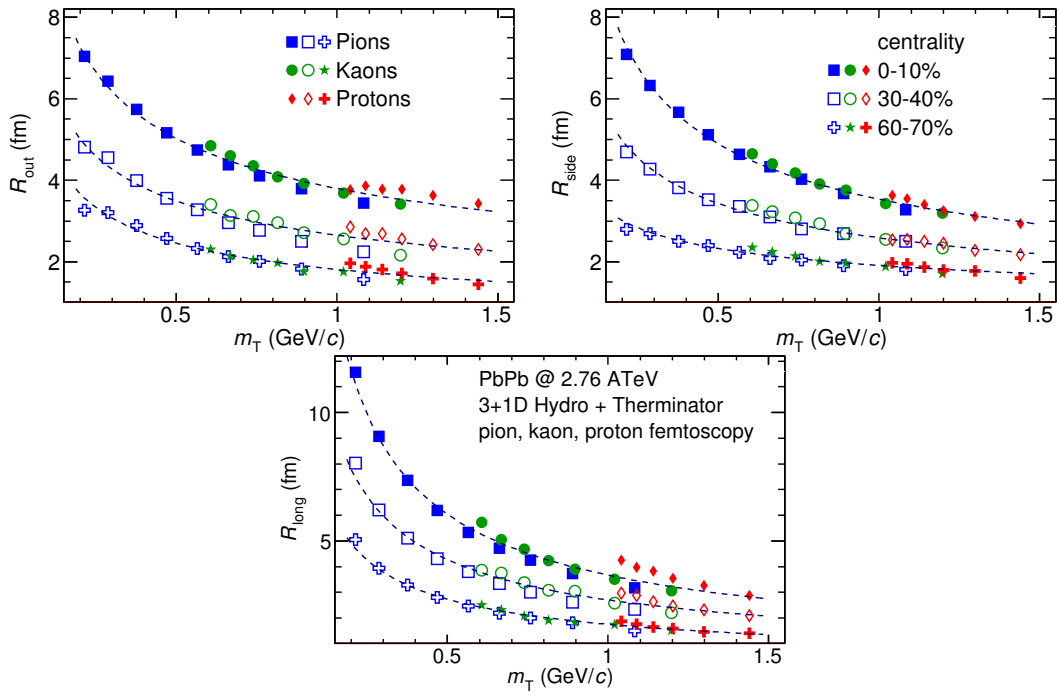


Figure 4.9: The results from the calculations for the pions, kaons and protons in for the three centralities presented on the common plot. One can notice that radii for particular centralities and different particle types follow the common power-law scaling. [30].

4.2.2 Scaling of one-dimensional radii

To the one-dimensional correlation function, the corresponding function in the PRF given by the Eq. 3.18 was fitted. The results from those fits are presented in the upper left plot in the Fig. 4.10. One immediately notices, that there is no common scaling of R_{inv} for different kind of particles. In the Fig. 4.9 the radii in the outward direction for the pions, kaons and protons for the same m_T are similar. However, when one performs a transition from the LCMS to the PRF, the R_{out} radius grows:

$$R_{out}^* = \gamma_T R_{out}, \quad (4.2)$$

where $\gamma_T = m_T/m$. For the lighter particles, the γ_T is much larger, hence the bigger growth of the R_{out} and the overall radius. This is visible in the Fig. 4.10 (top left), where the radii in the PRF for the lighter particles are bigger than for the heavier ones in case of the same m_T range.

In the Fig. 4.9 there is visible scaling in the outward, sideward and longitudinal direction. Hence one can expect an appearance of such scaling in a direction-averaged radius calculated in the LCMS. This radius is presented in the Fig. 4.10 (bottom) and indeed the R_{LCMS} exhibits power-law scaling with the m_T .

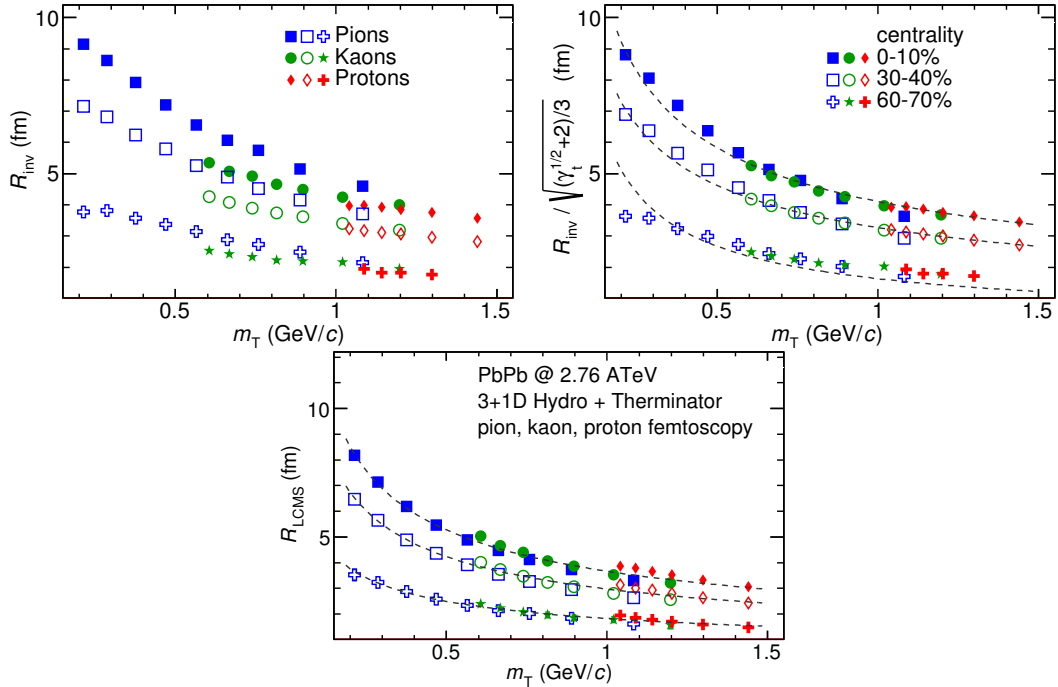


Figure 4.10: Top left: one-dimensional radius for pions, kaons and protons calculated in the PRF. Top right: the R_{inv} scaled by the proposed factor. Bottom: averaged one-dimensional radius in the LCMS for pions, kaons and protons. Only three centrality bins are shown for the better readability [30].

937 One can try to account the effect of an increase of the radii in the outward
 938 direction by using the appropriate scaling factor. In the Fig. 4.10 (top right) there
 939 are femtoscopic radii in the LCMS divided by the proposed scaling factor:

$$f = \sqrt{(\sqrt{\gamma_T} + 2)/3} . \quad (4.3)$$

940 The radii for pions, kaons and protons in the PRF after the division by f are
 941 following the power-law with the accuracy of 10%.

942 4.3 Discussion of the results

943 The femtoscopic radii obtained from the three-dimensional correlation func-
 944 tion fitting exhibit the m_T dependence described by the power law (Eq. 4.1). This
 945 scaling is preserved quite well with accuracy <10%. Observation of such scaling
 946 in a femtoscopic radii is a strong signal of appearance of a collective behaviour of
 947 a particle-emitting source created in the collision. The data used in the analysis
 948 was coming from the hydrodynamic model, hence one can indeed expect the
 949 appearance of this scaling. However, the results for pion femtoscopy from the
 950 ALICE at LHC are consistent with the data from analysis performed in this thesis
 951 (Fig. 4.6). This is a confirmation of an applicability of hydrodynamic models in a
 952 description of an evolution of a quark-gluon plasma.

953 The β parameter calculated in the fitting of the power-law to the femtoscopic
 954 radii is in the order of 0.5 in case of the radii in the transverse plane. This value is
 955 consistent with the hydrodynamic predictions. In case of longitudinal radii, the
 956 exponent is bigger (greater than 0.7), which is an indication of a strong transversal
 957 expansion in the system [28].

958 A scaling described above is visible in the LCMS, however due to limited stat-
 959 istics, analysis in this reference frame is not always possible. In such case one per-
 960 forms calculations in the PRF. The m_T scaling in the PRF is not observed - this has
 961 the trivial kinematic origin. A transition from the PRF to LCMS causes growth
 962 of the radius in the outward direction and the common power-law scaling for
 963 different particles breaks due to differences in the $\gamma_T(m_T)$ for different particle
 964 types. However one can try to deal with the radius growth and restore the scal-
 965 ing by multiplying the radii R_{inv} by an approximate factor $\sqrt{(\sqrt{\gamma_T} + 2)/3}$. The
 966 scaled R_{inv} are following the power-law and could be used as a verification of
 967 hydrodynamic behaviour in the investigated particle source.

968 The hadronic evolution and freeze-out in the THERMINATOR is followed
 969 by the resonance propagation and decay phase. A good accuracy of a scaling
 970 with the power-law indicated that the inclusion of the resonances does not
 971 break the m_T scaling. However, recent calculations including also hadron
 972 rescattering phase indicate that the scaling between pions and kaons is broken
 973 at the LHC [31].

974 Conclusions

975 This thesis presents the results of the two-particle femtoscopy of different
976 particle kinds produced in Pb-Pb collisions at the centre of mass energy
977 $\sqrt{s_{NN}} = 2.76$ TeV. The analysed data was generated by the THERMINATOR
978 model using the (3+1)-dimensional hydrodynamic model.

979 The momentum correlations were studied for three different types of particle
980 pairs: pions, kaons and protons. The data was analyzed for eight different sets
981 of initial conditions corresponding the following centrality ranges: 0-5%, 0-10%,
982 10-20%, 20-30%, 30-40%, 40-50%, 50-60% and 60-70%. The correlation functions
983 were calculated for the nine k_T bins from 0.1 GeV/c to 1.2 GeV/c. The cal-
984 culations were performed using spherical harmonics decomposition of a three-
985 dimensional correlation function. Using this approach, one can obtain full three-
986 dimensional information about the source size using only the three coefficients:
987 $\Re C_0^0$, $\Re C_2^0$ and $\Re C_2^2$. To perform further quantitative analysis, the femtoscopic
988 radii were extracted through fitting.

989 The calculated correlation functions show expected increase of a correlation
990 at low relative momenta in case of identical bosons (pions and kaons) and the
991 decrease for the identical fermions (protons) respectively. This effect is especially
992 visible in the first spherical harmonic coefficient $\Re C_0^0$. The other two components
993 $\Re C_2^0$ and $\Re C_2^2$ are non-vanishing and are providing information about the ratios
994 of radii in the outward, sideward and longitudinal directions.

995 An increase of width of a correlation function with the peripherality of a col-
996 lision and the k_T is observed for pions, kaons and protons. This increase of femto-
997 scopic radii (proportional to the inverse of width) with the k_T is related with the
998 m_T scaling predicted by the hydrodynamic calculations.

999 Hydrodynamic equations are predicting appearance of femtoscopic radii
1000 common scaling for different kinds of particles with the $m_T^{-0.5}$ in the LCMS.
1001 In the results in this work, a common scaling for different particle types is
1002 observed in the LCMS in the outward, sideward and longitudinal direction. The
1003 direction-averaged radius R_{LCMS} also shows this power-law behaviour. The
1004 fitting of a power law $\alpha m_T^{-\beta}$ to the femtoscopic radii yielded the information,
1005 that the β exponent for the outward and sideward direction is in order of 0.5,
1006 which is consistent with the hydrodynamic predictions. For the longitudinal
1007 direction, the β is bigger (>0.7) than in the other directions which is an indication
1008 of a strong transverse flow. Femtoscopic radii in LCMS are following the

1009 power-law scaling with the accuracy <5% for pions and kaons, and <10% in case
1010 of protons.

1011 In case of the one-dimensional radii R_{inv} calculated in the PRF, no common
1012 scaling is observed. This is a consequence of a transition from the LCMS to the
1013 PRF, which causes the growth of radius in the outward direction and breaks the
1014 scaling for different particles. However, one can try to correct the influence of
1015 the R_{out} growth with an approximate factor $\sqrt{(\sqrt{\gamma_T} + 2)/3}$. After the division
1016 of the R_{inv} by the proposed factor, the scaling is restored with an accuracy <10%.
1017 In this way, the experimentally simpler measure of the one-dimensional radii can
1018 be used as a probe for the hydrodynamic collectivity.

1019 The THERMINATOR model includes hydrodynamic expansion, statistical had-
1020 ronization, resonance propagation and decay afterwards. The m_T scaling is pre-
1021 dicted from the pure hydrodynamic calculations. However, this study shows,
1022 that influence of the resonances on this scaling is less than 10%.

1023

Bibliography

- 1024 [1] Standard Model of Elementary Paticles - Wikipedia, the free encyclopedia
1025 http://en.wikipedia.org/wiki/standard_model.
- 1026 [2] R. Aaij et al. (LHCb Collaboration). Observation of the resonant character of
1027 the $z(4430)^-$ state. *Phys. Rev. Lett.*, 112:222002, Jun 2014.
- 1028 [3] Donald H. Perkins. *Introduction to High Energy Physics*. Cambridge University Press,
1029 fourth edition, 2000. Cambridge Books Online.
- 1030 [4] G. Odyniec. *Phase Diagram of Quantum Chromo-Dynamics* - course at Faculty
1031 of Physics, Warsaw University of Technology, Jun 2012.
- 1032 [5] J. Beringer et al. (Particle Data Group). The Review of Particle Physics. *Phys.
1033 Rev.*, D86:010001, 2012.
- 1034 [6] Z. Fodor and S.D. Katz. The Phase diagram of quantum chromodynamics.
1035 2009.
- 1036 [7] F. Karsch. Lattice results on QCD thermodynamics. *Nuclear Physics A*, 698(1-
1037 4):199 – 208, 2002.
- 1038 [8] Adam Kisiel. *Studies of non-identical meson-meson correlations at low relative ve-
1039 locities in relativistic heavy-ion collisions registered in the STAR experiment*. PhD
1040 thesis, Warsaw University of Technology, Aug 2004.
- 1041 [9] J. Bartke. *Relativistic Heavy Ion Physics*. World Scientific Pub., 2009.
- 1042 [10] W. Florkowski. *Phenomenology of Ultra-Relativistic Heavy-Ion Collisions*.
1043 World Scientific, 2010.
- 1044 [11] Science Grid This Week, October 25, 2006 - Prob-
1045 ing the Perfect Liquid with the STAR Grid
1046 http://www.interactions.org/sgtw/2006/1025/star_grid_more.html.
- 1047 [12] K. Grebieszkow. Fizyka zderzeń ciężkich jonów,
1048 <http://www.if.pw.edu.pl/~kperl/hip/hip.html>.
- 1049 [13] Ulrich W. Heinz. From SPS to RHIC: Maurice and the CERN heavy-ion
1050 programme. *Phys.Scripta*, 78:028005, 2008.

- 1051 [14] J. Adams et al. Identified particle distributions in pp and Au+Au collisions
1052 at $s(\text{NN})^{**}(1/2) = 200 \text{ GeV}$. *Phys.Rev.Lett.*, 92:112301, 2004.
- 1053 [15] G. David, R. Rapp, and Z. Xu. Electromagnetic Probes at RHIC-II. *Phys.Rept.*,
1054 462:176–217, 2008.
- 1055 [16] A. Marin et al. Dilepton measurements with CERES. *PoS*, CPOD07:034,
1056 2007.
- 1057 [17] J. Adams et al. Experimental and theoretical challenges in the search for the
1058 quark gluon plasma: The STAR Collaboration’s critical assessment of the
1059 evidence from RHIC collisions. *Nucl.Phys.*, A757:102–183, 2005.
- 1060 [18] Adam Kisiel, Tomasz Taluc, Wojciech Broniowski, and Wojciech
1061 Florkowski. THERMINATOR: THERMal heavy-IoN generATOR. *Comput.Phys.Commun.*, 174:669–687, 2006.
- 1063 [19] Mikolaj Chojnacki, Adam Kisiel, Wojciech Florkowski, and Wojciech Bro-
1064 niowski. THERMINATOR 2: THERMal heavy IoN generATOR 2. *Comput.Phys.Commun.*, 183:746–773, 2012.
- 1066 [20] I. et al (BRAHMS Collaboration) Bearden. Charged meson rapidity distri-
1067 butions in central Au + Au collisions at $\sqrt{s_{\text{NN}}} = 200 \text{ GeV}$. *Phys. Rev. Lett.*,
1068 94:162301, Apr 2005.
- 1069 [21] W. Israel and J.M. Stewart. Transient relativistic thermodynamics and kin-
1070 etic theory. *Annals of Physics*, 118(2):341 – 372, 1979.
- 1071 [22] Piotr Bożek. Flow and interferometry in (3 + 1)-dimensional viscous hydro-
1072 dynamics. *Phys. Rev. C*, 85:034901, Mar 2012.
- 1073 [23] K. Kovtun, P. D. T. Son, and A. O. Starinets. Viscosity in strongly interacting
1074 quantum field theories from black hole physics. *Phys. Rev. Lett.*, 94:111601,
1075 Mar 2005.
- 1076 [24] Fred Cooper and Graham Frye. Single-particle distribution in the hydro-
1077 dynamic and statistical thermodynamic models of multiparticle production.
1078 *Phys. Rev. D*, 10:186–189, Jul 1974.
- 1079 [25] Adam Kisiel. Nonidentical-particle femtoscopy at $\sqrt{s_{\text{NN}}} = 200 \text{ GeV}$ in hy-
1080 drodynamics with statistical hadronization. *Phys. Rev. C*, 81:064906, Jun
1081 2010.
- 1082 [26] Adam Kisiel and David A. Brown. Efficient and robust calculation of femto-
1083 scopic correlation functions in spherical harmonics directly from the raw
1084 pairs measured in heavy-ion collisions. *Phys.Rev.*, C80:064911, 2009.
- 1085 [27] S. Pratt. Pion Interferometry for Exploding Sources. *Phys.Rev.Lett.*, 53:1219–
1086 1221, 1984.

- 1087 [28] S.V. Akkelin and Yu.M. Sinyukov. The HBT-interferometry of expanding
1088 inhomogeneous sources. *Z.Phys.*, C72:501–507, 1996.
- 1089 [29] K. Aamodt et al. Two-pion Bose-Einstein correlations in central Pb-Pb colli-
1090 sions at $\sqrt{s_{NN}} = 2.76$ TeV. *Phys.Lett.*, B696:328–337, 2011.
- 1091 [30] A. Kisiel, M. Galazyn, and P. Bozek. Pion, kaon, and proton femtoscopy in
1092 Pb-Pb collisions at $\sqrt{s_{NN}}=2.76$ TeV modeled in 3+1D hydrodynamics. 2014.
- 1093 [31] V.M. Shapoval, P. Braun-Munzinger, Iu.A. Karpenko, and Yu.M. Sinyukov.
1094 Femtoscopy correlations of kaons in $Pb + Pb$ collisions at LHC within hy-
1095 drokinetic model. 2014.

¹⁰⁹⁶ List of Figures

1097	1.1	The Standard Model of elementary particles [1].	3
1098	1.2	A string break and a creation of a pair quark-anti-quark [4].	5
1099	1.3	The coupling parameter α_s dependence on four-momentum transfer Q^2 [5].	6
1100	1.4	The QCD potential for a pair quark-antiquark as a function of distance for different temperatures. A value of a potential decreases with the temperature [4].	6
1101	1.5	A number of degrees of freedom as a function of a temperature [7].	7
1102	1.6	Phase diagram coming from the Lattice QCD calculations [8].	8
1103	1.7	Left: stages of a heavy ion collision simulated in the UrQMD model. Right: schematic view of a heavy ion collision evolution [8].	9
1104	1.8	Overlapping region which is created in heavy ion collisions has an almond shape. Visible x-z plane is a <i>reaction plane</i> . The x-y plane is a <i>transverse plane</i> . The z is a direction of the beam [11].	11
1105	1.9	Cross-section of a heavy ion collision in a transverse plane. Ψ_R is an angle between transverse plane and the reaction plane. The b parameter is an <i>impact parameter</i> - a distance between centers of nuclei during a collision. An impact parameter is related with the centrality of a collision and a volume of the quark-gluon plasma [12].	12
1106	1.10	<i>Lower:</i> The elliptic flow v_2 follows the hydrodynamical predictions for an ideal fluid perfectly. Note that > 99% of all final hadrons have $p_T < 1.5$ GeV/c. <i>Upper left:</i> The v_2 plotted versus transverse kinetic energy $KE_T = m_T - m_0 = \sqrt{p_T^2 + m_0^2} - m_0$. The v_2 follows different universal curves for mesons and baryons. <i>Upper right:</i> When scaled by the number of valence quarks, the v_2 follows the same universal curve for all hadrons and for all values of scaled transverse kinetic energy [13].	13
1107	1.11	Invariant yield of particles versus transverse mass $m_T = \sqrt{p_T^2 + m_0^2}$ for π^\pm , K^\pm , p and \bar{p} at mid-rapidity for p+p collisions (bottom) and Au+Au events from 70-80% (second bottom) to 0-5% (top) centrality [14].	14

1128	1.12 Thermal photons spectra for the central Au+Au collisions at	
1129	$\sqrt{s_{NN}} = 200$ GeV at computed within different hydrodynamical	
1130	models compared with the pQCD calculations (solid line) and	
1131	experimental data from PHENIX (black dots) [15].	15
1132	1.13 Left: Invariant mass spectrum of e^+e^- pairs in Pb+Au collisions	
1133	at 158A GeV compared to the sum coming from the hadron decays	
1134	predictions. Right: The expectations coming from model calcula-	
1135	tions assuming a dropping of the ρ mass (blue) or a spread of the	
1136	ρ width in the medium (red) [16].	16
1137	1.14 Azimuthal angle difference $\Delta\phi$ distributions for different colliding	
1138	systems at $\sqrt{s_{NN}} = 200$ GeV. Transverse momentum cut: $p_T > 2$	
1139	GeV. For the Au+Au collisions the away-side jet is missing [17]. . .	17
1140	3.1 Bertsch-Pratt direction naming convention used in heavy ion col-	
1141	lision.	23
1142	3.2 The pair wave function is a superposition of all possible states. In	
1143	case of particle interferometry it includes two cases: particles with	
1144	momenta p_1, p_2 registered by detectors A, B and p_1, p_2 registered	
1145	by B, A respectively.	24
1146	3.3 An averaged three-dimensional Gaussian source function with dif-	
1147	ferent widths was averaged into one-dimensional function. To il-	
1148	lustrate deformations, one-dimensional Gaussian distribution was	
1149	fitted.	27
1150	3.4 Correlation function width dependence on total pair momentum.	
1151	Pion pairs with a large total momentum are more correlated [27]. .	31
1152	4.1 Spherical harmonics coefficients of the two-pion correlation func-	
1153	tion. From the top left: $\Re C_0^0$, $\Re C_2^0$ and $\Re C_2^2$. Only few centrality	
1154	bins are presented for increased readability.	34
1155	4.2 Spherical harmonics coefficients of the two-kaon correlation func-	
1156	tion. From the top left: $\Re C_0^0$, $\Re C_2^0$ and $\Re C_2^2$. Only few centrality	
1157	bins are presented for increased readability. The $\Re C_2^2$ is noisy, but	
1158	one can still notice that it differs from zero and is becoming negative. .	35
1159	4.3 Spherical harmonics coefficients of the two-proton correlation	
1160	function. From the top left: $\Re C_0^0$, $\Re C_2^0$ and $\Re C_2^2$. Only few	
1161	centrality bins are presented for increased readability. The $\Re C_2^0$	
1162	and $\Re C_2^2$ are noisy, but one can still notice, that they differ from	
1163	zero and are becoming positive.	36
1164	4.4 One-dimensional correlation function for pions(top left), kaons	
1165	(top right) and protons (bottom) for different centralities.	37

1166	4.5	One-dimensional correlation functions for pions, kaons and protons, for the same centrality bin and different k_T ranges. The plot was zoomed in to the region which illustrates the k_T dependence in the best way. Only few of the calculated ranges are presented for better readability.	38
1167	4.6	Femtoscopic radii in LCMS coming from two-pion correlation functions for all centrality bins as a function of m_T . The dashed lines are power-law fits. The most central collisions (0-5%) are compared to the results from ALICE [29]. The two datasets are shifted to the right for visibility [30].	39
1168	4.7	Femtoscopic radii extracted from two-kaon correlation functions for different centrality bins as a function of m_T . [30].	40
1169	4.8	Femtoscopic radii extracted from two-proton correlation functions for different centrality bins as a function of m_T . [30].	41
1170	4.9	The results from the calculations for the pions, kaons and protons in for the three centralities presented on the common plot. One can notice that radii for particular centralities and different particle types follow the common power-law scaling. [30].	42
1171	4.10	Top left: one-dimensional radius for pions, kaons and protons calculated in the PRF. Top right: the R_{inv} scaled by the proposed factor. Bottom: averaged one-dimensional radius in the LCMS for pions, kaons and protons. Only three centrality bins are shown for the better readability [30].	43
1172			
1173			
1174			
1175			
1176			
1177			
1178			
1179			
1180			
1181			
1182			
1183			
1184			
1185			
1186			
1187			
1188			